The Astrophysical Journal, 922:73 (18pp), 2021 November 20 https://doi.org/10.3847/1538-4357/ac1862

Global Distribution of the Solar Wind Speed Reconstructed from Improved Tomographic Analysis of Interplanetary Scintillation Observations between 1985 and 2019

Munetoshi Tokumaru, Ken'ichi Fujiki, Masayoshi Kojima, and Kazumasa Iwai
Institute for Space-Earth Environmental Research, Nagoya University, Furo-cho, Chikusa-ku, Nagoya 464-8601, Japan; tokumaru@isee.nagoya-u.ac.jp
Received 2021 April 15; revised 2021 July 21; accepted 2021 July 26; published 2021 November 23

Abstract

Computer-assisted tomography (CAT) for interplanetary scintillation (IPS) observations enables the determination of the global distribution of solar wind speed. We compared solar wind speeds derived from the CAT analysis of IPS observations between 1985 and 2019 with in situ observations conducted by the near-Earth and Ulysses spacecraft. From this comparison, we found that solar wind speeds from the IPS observations for 2009–2019 were systematically higher than the in situ observations, whereas those for the period until 2008 were in good agreement with the in situ observations. Further, we found that the discrepancy between IPS and the in situ observations is improved by changing the power index of the empirical relation between the solar wind speed and density fluctuations. The CAT analysis using an optimal value for the power index determined from the comparison between IPS and in situ observations revealed long-term variations in the solar wind speed distribution over three cycles, leading to a better understanding of the time-varying global heliosphere. We found that polar solar winds become highly anisotropic at the Cycle 24/25 minimum, which is a peculiar aspect of this minimum. The IPS observations showed general agreement with the Parker Solar Probe observations around the perihelion of Orbit 1; this supports the reliability of the CAT analysis. The results of this study suggest that the physical properties of solar wind microturbulence may vary with a long-term decline in the solar activity, which provides important implication on the solar wind acceleration.

Unified Astronomy Thesaurus concepts: Solar magnetic fields (1503); Solar wind (1534); Interplanetary scintillation (828); Solar cycle (1487)

1. Introduction

Solar wind is a turbulent plasma flow emanating from the Sun, and its properties fluctuate over a wide range of spatial and temporal scales (e.g., Schwenn & Marsch 1991; Bruno & Carbone 2005). Solar wind turbulence provides information on the formation of solar wind, whose physical process remains an unsolved question, and it may play a vital role in accelerating solar wind. Shoda et al. (2019) showed that the density fluctuations of the solar wind driven by the parametric decay instability significantly enhance the efficiency of Alfvén wave reflection, which results in the effective heating and acceleration of solar wind. Density irregularities in the solar wind cause interplanetary scintillation (IPS), which is a rapid intensity variation of radio waves from a compact source. The IPS serves as a useful probe for investigating solar wind turbulence and its motion (Hewish et al. 1964; Coles 1978): the temporal spectrum of IPS for a high-frequency range above the Fresnel frequency reflects the spatial spectrum of the solar wind density fluctuations, and the solar wind speed can be derived by measuring the time lag between the IPS patterns at separated sites. In our earlier study, the magnitude of solar wind density fluctuations ΔN_e was found to be closely related to the solar wind speed V, and the relation $\Delta N_e \propto V^{-0.5}$ was deduced based on the tomographic analysis of the IPS observations (Asai et al. 1998; Tokumaru et al. 2012). Although the physical meaning of this relationship has yet to be fully understood, the fractional density fluctuations $\Delta N_e/N_e$ are given as $\Delta N_e/N_e \propto V^{1.5}$ if the momentum flux N_eV^2 is uniform among different speed flows (Steinitz & Eyni 1980; Mullan 1983). This suggests that $\Delta N_e/N_e$ in the fast wind is greater than that in the slow wind. The correlation between $\Delta N_e/N_e$ and V may be regarded as observational evidence that supports the Alfvén wave driven solar wind model mentioned above. The IPS observations represent small-scale (∼100 km) density fluctuations, i.e., microturbulence, which were inaccessible to in situ measurements in the past owing to an insufficient temporal resolution.

The IPS observations with many lines of sight allow determining the global distribution of solar wind. Here, the effect of line-of-sight (LOS) integration, which is inherent in IPS observations, must be treated carefully. The LOS integration effect is known to sometimes significantly bias the solar wind speed measured by the IPS. We used the computer-assisted tomography (CAT) method to correct the LOS integration effect and retrieve an intrinsic distribution of the solar wind speed from IPS observations (e.g., Jackson et al. 1998; Kojima et al. 1998, 2007). A precise understanding of ΔN_e is required in the CAT analysis of IPS observations because it provides the weighting function for a LOS integration. The relationship $\Delta N_e \propto V^{-0.5}$ was employed in our CAT code. Our earlier study demonstrated that solar wind speed data derived from the CAT analysis of IPS observations are compatible with the in situ observations (Fujiki et al. 2003; Kojima et al. 2007). However, a non-negligible discrepancy was revealed from a comparison between the CAT analysis and in situ observations for recent periods, as mentioned below (see also Sokół et al. 2020). The solar wind speeds derived from the CAT analysis were found to be systematically higher than the in situ measurements at 1 au in solar Cycle 24 (after 2009). IPS is presently the only method for measuring the solar wind speed out of the ecliptic, and earlier studies using our IPS observations revealed the global feature of the heliosphere drastically varying with the solar cycle (e.g., Tokumaru et al. 2010, 2012, 2015, 2018). Further, our IPS

observations provided crucial information in interpreting observations of the interstellar energetic neutral atoms, which act as a useful probe for investigating the heliospheric boundary region (e.g., McComas et al. 2020; Sokół et al. 2020). Therefore, an improvement of the CAT analysis is highly desired to gain a better understanding of the global heliosphere. Moreover, the improvement of the CAT analysis may result in accurate modeling of ΔN_e, which leads to gain a deeper insight into physical processes of the solar wind microturbulence.

In this study, we investigated the cause of the discrepancy between the CAT analysis and in situ observations in and out of the ecliptic plane, and we found that this discrepancy was significantly improved by adjusting the ΔN_e–V relation used in the CAT analysis. We analyzed IPS observations made at the Institute for Space-Earth Environmental Research (ISEE) of Nagoya University using the CAT analysis optimized for in situ measurements, and we addressed long-term variations in the global distribution of the solar wind speed during Cycles 22–24. Further, we also compared the CAT analysis with the Parker Solar Probe (PSP; Fox et al. 2016) observations for the first orbit in 2018 (Orbit 1). The remainder of this paper is organized as follows. In Section 2, we briefly describe the IPS observations at ISEE and the CAT analysis. In Section 3, we present a comparison between the CAT analysis of the IPS observations and the in situ observations obtained by the near-Earth and out-of-ecliptic spacecraft for the period between 1985 and 2019. We examine the effects of the number of LOS and power-law index of the ΔN_e–V relationship as a cause for discrepancies between IPS and in situ observations. In Section 4, we present the solar cycle variations in the global distribution of the solar wind speed derived from the improved CAT analysis. In Section 5, we present a comparison of IPS and PSP observations. In Section 6, we summarize and discuss the results of this study.

2. Observations

2.1. IPS Observations

IPS observations have been conducted since 1983 at ISEE using the 327 MHz multi-station system (Kojima & Kakinuma 1990; Tokumaru 2013). The solar wind speeds are derived from the cross-correlation analysis of the IPS observed simultaneously at three or four stations. Solar wind speed data from the ISEE IPS observations are available on http://stsw1.isee.nagoya-u.ac.jp/vlist. In this study, we analyzed the solar wind speed data obtained for 1985–2019 using the CAT method. This analysis period covers three solar cycles: Cycle 21/22 minimum to Cycle 24/25 minimum. We note that the solar wind speed data are unavailable in winter owing to snow at the observatories, and data collected in 2010 were very few owing to a system upgrade; this is insufficient to obtain meaningful results from the CAT analysis. A more detailed description of ISEE IPS observations has been presented in our earlier studies (e.g., Tokumaru et al. 2010, 2012, 2015, 2017, 2018).

2.2. CAT Analysis

Among several versions of the CAT method, we employed the time-sequence (TS) CAT method (Fujiki et al. 2003; Kojima et al. 2007), as with earlier studies (e.g., Tokumaru et al. 2010). In TS-CAT, a seamless large map composed of consecutive solar rotations is used as a reference surface that provides a distribution of the solar wind speed V, and the lines of sight for IPS observations are projected onto this surface by assuming that the solar wind flows radially at a constant speed. This treatment allows the retrieval of quasi-stationary solar wind structures, which can change between rotations. In the TS-CAT, the solar wind structure is assumed to evolve slowly, and the timescales of the structural evolution must not be much shorter than the solar rotation period. Therefore, the TS-CAT cannot retrieve rapidly evolving structures, which frequently occur at the solar maximum. The reference surface, i.e., the source surface, was assumed to be located at 2.5 R_S. The seamless map of the source surface for a given year included 11 solar rotations in our analysis.

Using the map of the solar wind speed, the effect of LOS integration was corrected through the following iterative procedure. First, the cross-correlation function C_z is integrated along the LOS for a given IPS observation as

$$C(\tau) = \int_0^{z_{\max}} w(z) C_z(\tau, V(z)\cos(\theta(z))dz, \tag{1}$$

where τ, $\theta(z)$, and z denote the time delay, angle between the solar wind flow direction (radial direction) and the direction normal to LOS, and the distance along LOS, respectively, and $w(z)$ denotes the weighting function of the IPS given by Young (1971)

$$w(z) = \Delta N_e^2 \frac{1}{r^4} \int_0^{\infty} dq \sin^2\left(\frac{q^2\lambda z}{4\pi}\right)\exp\left(-\frac{\Theta^2 q^2 z^2}{2}\right) q^{1-\beta}, \tag{2}$$

where r, q, λ, Θ, and β denote the radial distance from the Sun, wavenumber, radio wavelength (0.92 m), source size, and spectral index of density turbulence, respectively. In this formula, we assume that ΔN_e is distributed as r^{-2}. We employ a Gaussian function with an e-folding width of the Fresnel scale and a shifted peak at a time lag depending on V as C_z. The solar wind speeds along the projected LOS on the source surface were used for V in this integration. The value of ΔN_e must be given to calculate $C(\tau)$. One of the methods uses a model that prescribes ΔN_e as a function of V (e.g., Kojima et al. 1998; Tokumaru et al. 2010; hereinafter referred to as the conventional method). Another method uses g-values which represent the relative variation of an integrated ΔN_e level for a given LOS to deconvolve LOS integrations of V and ΔN_e simultaneously (e.g., Asai et al. 1998; Tokumaru et al. 2012; hereinafter referred to as the simultaneous deconvolution method). In the present study, we employ the conventional CAT, partly because it provides a better coverage for investigating global distribution of the solar wind speed over a long period. The simultaneous deconvolution method requires that both solar wind speed and g-value are available for the same LOS, and therefore the spatial coverage of the derived source surface map is reduced compared to that of the conventional CAT. Further, the analysis period of the simultaneous deconvolution method is limited to after 1997 when g-value data became available from ISEE IPS observations. Another reason why the conventional method is used here is that the discrepancy between IPS and in situ observations was not improved by the simultaneous deconvolution method but by the conventional method, as mentioned in Section 3.5. Since no theoretical model is currently available to prescribe ΔN_e, we employ an empirical relationship that assumes $\Delta N_e \propto V^{\alpha}$. In our earlier

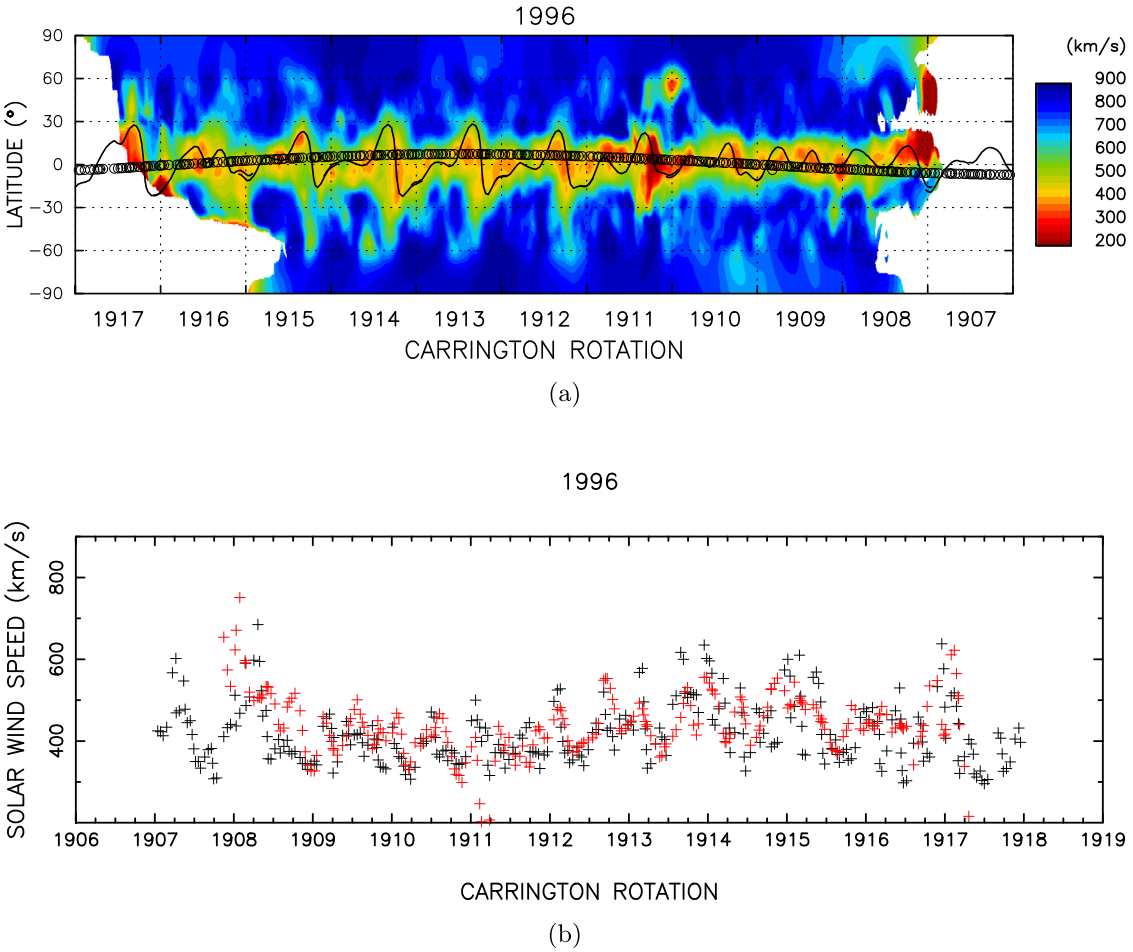

Figure 1. (a) Synoptic source surface map of the solar wind speed derived from the CAT analysis of IPS observations for 1996. The solid line indicates the magnetic neutral line from magnetograph observations at the Wilcox Solar Observatory (WSO). Open circles indicate the locations of the Earth projected onto the source surface. (b) Variations of the solar wind speeds derived from IPS observations along the trajectory of Earth (red) and those from in situ observations at the Earth orbit, i.e., OMNI (black) for 1996.

studies, $\alpha = -0.5$ was used. Further, we assume that $\Theta = 0.1''$ for all sources, and $z_{\max} = 2$ au, $\beta = 3.3$ (Kolmogorov value). Next, a time lag corresponding to a peak of $C(\tau)$ is determined and converted to the solar wind speed $V_{\rm sim}$. Then, $V_{\rm sim}$ is compared with the observed speed $V_{\rm obs}$, and the values of V on the source surface are modified to reduce the difference between $V_{\rm sim}$ and $V_{\rm obs}$. These steps are repeated until the difference becomes sufficiently small. Finally, we obtain the solar wind speed data wherein the LOS integration effect is corrected when the iteration is completed.

2.3. In Situ Observations

For comparison with the IPS observations, we used the hourly averaged solar wind data derived from in-ecliptic plasma measurements at 1 au, called OMNI (King & Papitashvili 2005), and those derived from out-of-ecliptic measurements with the Ulysses spacecraft (Bame et al. 1992). These data were obtained from the COHOweb (https://omniweb.gsfc.nasa.gov/coho/). The OMNI data fully cover the analysis period, whereas the Ulysses data cover the period between 1990 and 2009. From the comparison, we optimized the CAT analysis to minimize discrepancies between IPS and in situ observations. Further, we used the solar wind data from in situ measurements with PSP for Orbit 1, which occurred in late 2018, for comparison. The hourly averaged PSP data were adopted via CDAweb (https://cdaweb.gsfc.nasa.gov/index.html/). The perihelion of Orbit 1 was located at 35.6 R_S, which is beyond the solar wind acceleration region. Therefore, the solar wind speeds derived from PSP observations for Orbit 1 should agree with those from the IPS observations. We examined the accuracy of the improved CAT analysis by comparing the PSP and IPS observations.

3. Comparison between IPS and In Situ Observations

3.1. IPS-OMNI Comparison

Figure 1(a) shows a synoptic map of the solar wind speed on the source surface derived from the TS-CAT analysis of IPS observations for 1996. We used $\alpha = -0.5$ to produce this map. In this figure, open circles indicate the locations of the OMNI measurements. Figure 1(b) shows a comparison between IPS and OMNI observations along the trajectory of OMNI for 1996. A positive correlation with a coefficient of 0.41 is obtained from this comparison. The corresponding level of significance of this correlation, i.e., the p-value is considerably smaller than 5%; hence, the null hypothesis is safely rejected.

We performed such a comparison for every year between 1985 and 2019 except for 2010, by employing the CAT analysis with $\alpha = -0.5$. We calculated dV and σ_V, which are the mean of the speed difference and the rms deviation for a

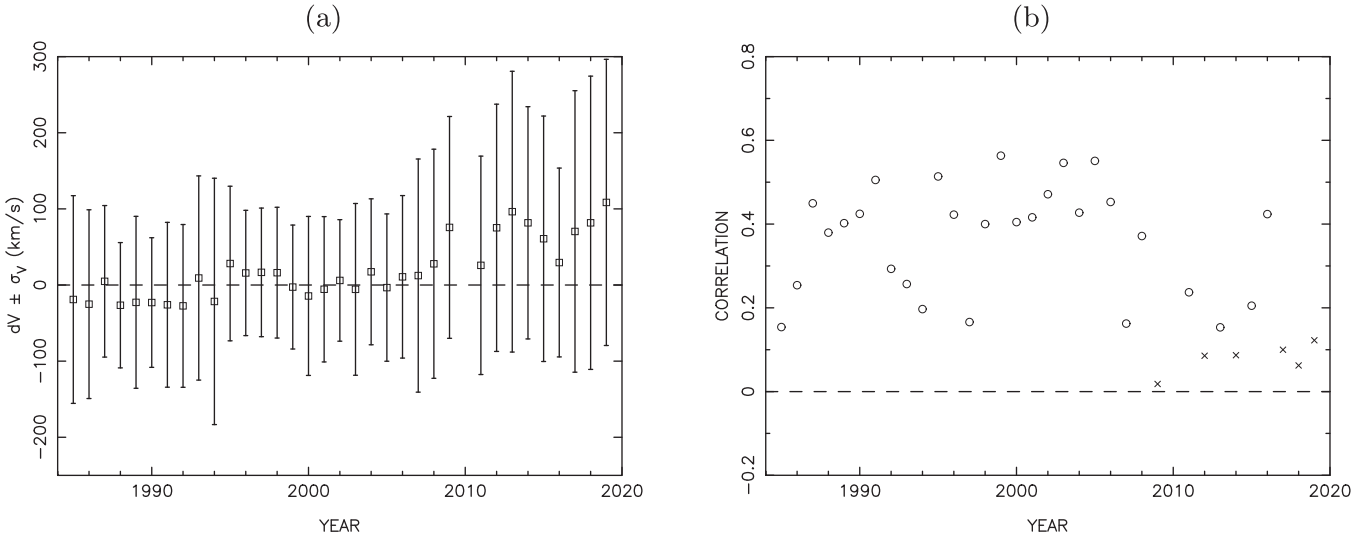

Figure 2. (a) dV (square) with $\pm\,\sigma_V$ (vertical bar), (b) correlation coefficients with $p < 0.05$ (circle) and those with $p > 0.05$ (cross) from IPS-OMNI comparison during 1985–2019.

given year in the analysis period; they are respectively given as follows:

$$dV = \frac{1}{N}\sum_{i=1}^{N}(V_{\rm IPS}(i) - V_{\rm SC}(i)), \tag{3}$$

$$\sigma_V = \sqrt{\frac{1}{N}\sum_{i=1}^{N}(V_{\rm IPS}(i) - V_{\rm SC}(i))^2}\,, \tag{4}$$

where $V_{\rm SC}$ and $V_{\rm IPS}$ denote the solar wind speeds derived from in situ observations (i.e., OMNI) and those from IPS observations along the trajectory of the spacecraft (i.e., Earth), respectively, and N denotes the number of data. Figure 2(a) shows the time variations of dV and σ_V during 1985–2019. The values of dV before 2008 fluctuate around 0 km s^{-1} within $\pm$20 km s^{-1}, and the average dV is -2.4 ± 18 km s^{-1} for the period 1985–2008. This implies that the CAT analysis provides solar wind speed data that are as reliable as the in situ measurements. However, the dV shifts to positive values after 2009, and the average value between 2009 and 2019 is 71 ± 26 km s^{-1}. Thus, CAT analysis overestimates the solar wind speed in the ecliptic plane in the recent period. In contrast, dV for 1985–1994 is systematically negative, which suggests that the CAT analysis underestimates the in-ecliptic wind speed by 18 km s^{-1} for this period. A similar increasing tendency was found in σ_V: the average values of σ_V for 1985–2008 and 2009–2019 were 108 ± 24 and 164 ± 24 km s^{-1}, respectively. The behavior of σ_V for 1985–1994 is different from that of dV, and the σ_V for this period exhibits a slightly larger value on average than that for 1995–2008.

Figure 2(b) shows the time variation of the correlation coefficients between IPS and OMNI observations for the analysis period. We calculated the p-values for observed correlations. Meaningful positive correlations that correspond to those with a p-value less than 5% ($p < 0.05$) are revealed for most of the years in this figure. The average value of the correlation coefficients over the analysis period was 0.31. The correlations were found to be greatly degraded in the recent period: 2009, 2014, and 2017–2019 in Cycle 24. The null hypothesis cannot be rejected safely for these years because $p > 0.05$. These correlation drops appear to be associated with positive deviations of dV from zero and increases in σ_V, as mentioned previously. Moderate drops in the correlation occurred in some other years: 1986, 1997, and 2007, and there were no associated changes in dV and σ_V. Further, we calculated correlation coefficients by selecting IPS data for a solar rotation with good coverage (e.g., >80% in 360 × 180 grid points) in the synoptic map, and we found that there was no significant improvement in the correlations for selected IPS data, although they achieved slightly higher coefficients on average compared to those obtained from all data.

3.2. IPS-Ulysses Comparison

Figure 3 shows the comparison between IPS and Ulysses observations for 1996 along the trajectory of the Ulysses spacecraft. The locations of Ulysses observations moved from the mid to low latitudes during this period, and the resultant transition from the fast wind to the slow wind is clearly demonstrated in this figure because the solar wind had a bimodal structure in 1996. The IPS observations show good agreement with Ulysses observations, and this suggests that the CAT analysis of IPS observations provides reliable estimates of the solar wind speed distribution not only for the in-ecliptic region but also for the out-of-ecliptic region. We calculated dV, σ_V, and the correlation coefficients in a way similar to the IPS-OMNI comparison, while the analysis period was between 1990 and 2009. Figure 4 shows the time variation of (a) dV, σ_V, and (b) correlation coefficients during the analysis period. The average values of dV and σ_V are -2.3 ± 33 km s^{-1} and 103 ± 23 km s^{-1}, respectively. The agreement between IPS and Ulysses observations is better than that between IPS and OMNI observations. This fact is ascribed to the recent period when an increasing tendency of dV and σ_V is found from the comparison between IPS and OMNI observations, which is not included here. No systematic change is revealed in Figure 4(a), and there are marked excursions of dV and σ_V to negative and larger values, respectively, in 1993 and 1994. The comparison between IPS and Ulysses observations yields meaningful correlation coefficients for most years, although there are significant drops in correlation for 1990 and 1994. This feature is consistent with

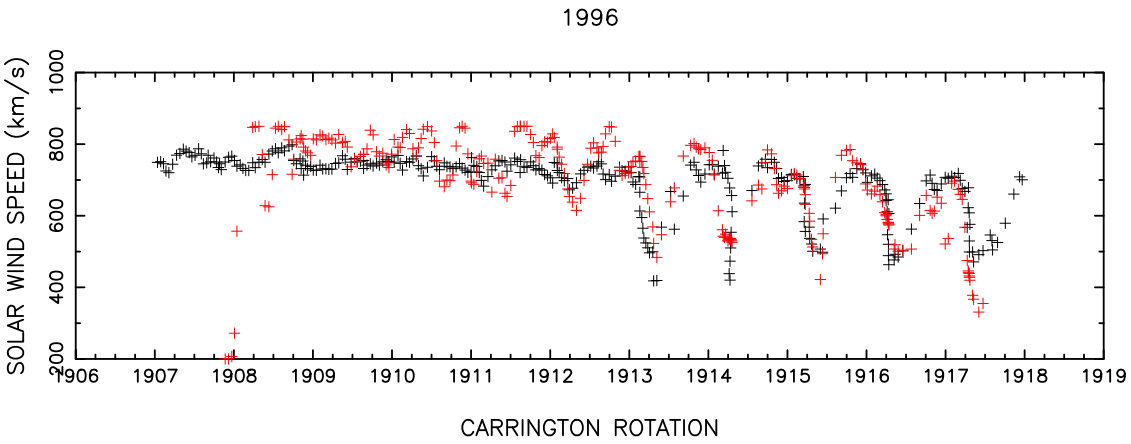

Figure 3. Variations of the solar wind speeds derived from IPS observations (red) along the trajectory of Ulysses and those from in situ observations conducted by Ulysses (black) for 1996.

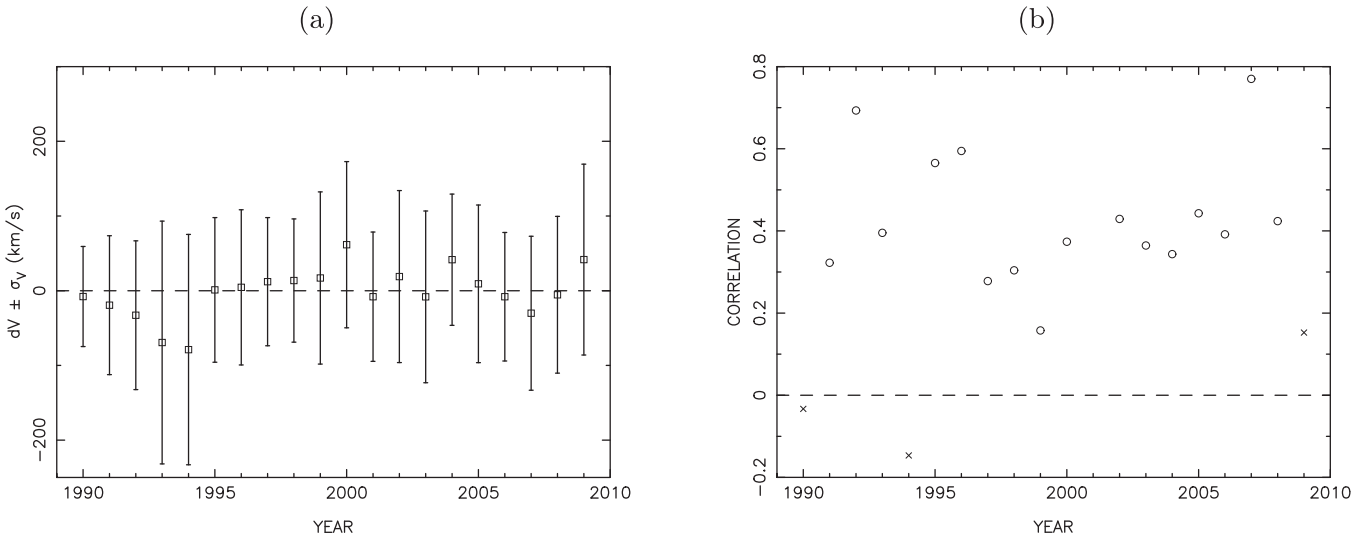

Figure 4. (a) dV (square) with $\pm\ \sigma_V$ (vertical bar), (b) correlation coefficients with $p < 0.05$ (circle) and those with $p > 0.05$ (cross) from IPS-Ulysses comparison during 1990–2009.

correlations obtained from the IPS-OMNI comparison. The average value of correlation coefficients over the analysis period is 0.38. The correlation drop for 1990 is likely caused by the insufficient number of data for comparison.

3.3. Possible Cause of Discrepancies in the Solar Wind Speed

3.3.1. Amount of Data

The amount of IPS data, i.e., the number of LOS used for the CAT analysis varies with the year depending on several factors such as degradation over time, maintenance and upgrading of the IPS system, and addition/deletion of the IPS antennas. Further, the long-term decline in the IPS level caused by the weakening of solar activity (Janardhan et al. 2015) can result in reduction of the amount of IPS data. Figure 5 shows the variation in the amount of IPS data during 1985–2019. The IPS data are composed of solar wind speed estimates derived from three-station measurements and those from two-station measurements. The former includes the estimation error of the solar wind speed, whereas the latter does not. In the CAT analysis,

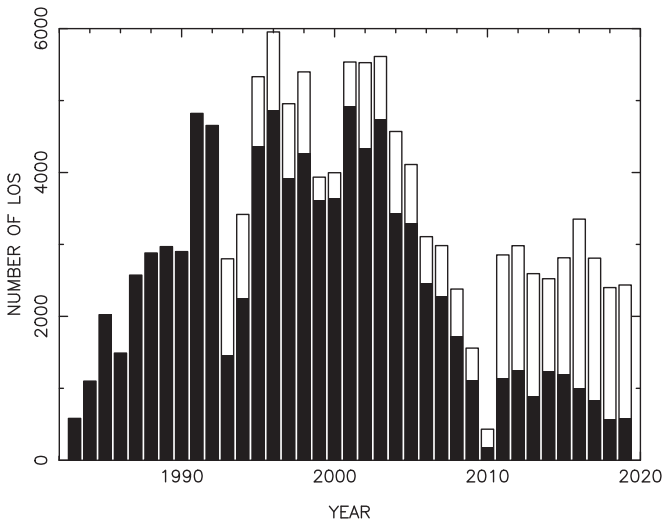

Figure 5. Yearly variation of the number of IPS data during 1985–2019. Solid and open bars correspond to the ones obtained from the three-station and two-station measurements, respectively.

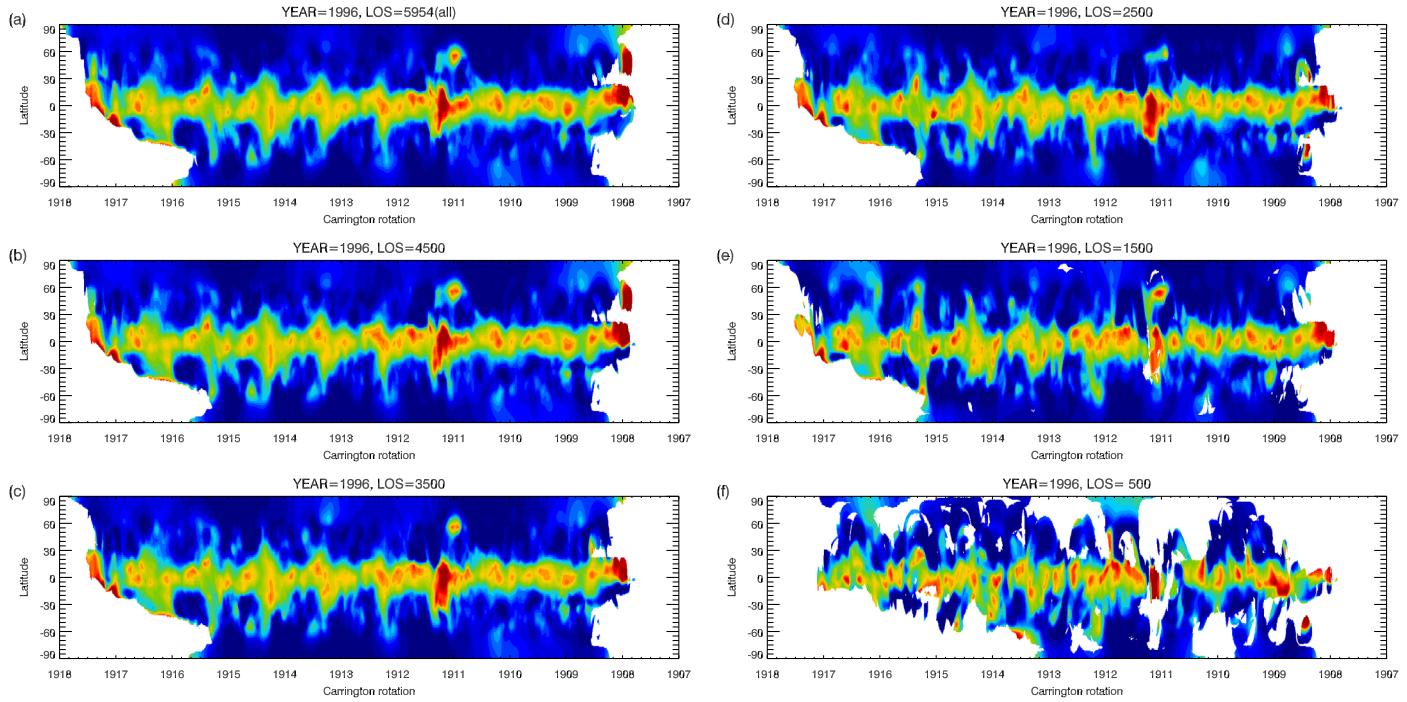

Figure 6. Solar wind speed maps derived from the CAT analysis using (a) all (5954), (b) 4500, (c) 3500, (d) 2500, (e) 1500, and (f) 500 of the IPS data for 1996.

only three-station data were used because they are more reliable than the two-station data. The numbers of IPS data near the beginning and end of the analysis period are significantly smaller than that of the mid-portion, particularly for the case of the three-station data. This is a possible cause for the worsened agreement between IPS and in situ (OMNI) observations in the recent period. To examine this possibility, we performed a simulation analysis using IPS observations as follows. First, we prepared IPS data sets whose amounts were reduced by extracting the data in a random manner. The number of LOS in the reduced IPS data changed from 5000 to 500 in increments of 500. Then, we performed the CAT analysis using the reduced IPS data sets for every year between 1985 and 2009. Finally, we compared the results with the OMNI observations and calculated dV and σ_V. Figure 6 shows the solar wind speed maps derived from the CAT analysis using the reduced IPS data sets for 1996. The numbers of LOS are 5954, 4500, 3500, 2500, 1500, and 500 for Figures 6(a)–(f), respectively. The bimodal feature of the solar wind speed distribution is discernible even for the case of 500 LOS, although its observation coverage becomes poor. A similarity was found between the results derived from IPS data with different numbers of LOS. This suggests that the CAT analysis is robust against changes in the number of LOS.

Figure 7 illustrates the variations in dV and σ_V with a decreasing number of the LOS. As shown in Figure 7(c), σ_V tends to rise to a larger value with a decrease in the number of LOS, and this is consistent with that observed for σ_V in the recent period. However, dV shown in Figure 7(b) tends to shift to a negative value as the number of LOS decreases, which is inconsistent with what was observed for dV after 2009. Hence, we consider that the reduced amount of IPS data cannot fully account for worsened agreement between IPS and OMNI observations, particularly for dV observed in the recent period.

3.3.2. Index α

Since the empirical relationship $\Delta N_e \propto V^{\alpha}$ is used as the weighting function, the index α is likely to influence the results of the CAT analysis. To examine the effect of the index α, we performed the CAT analysis using different values for α, and compared the results with in situ observations. Figure 8 shows the variations in dV and σ_V during 1985–2019 obtained from a comparison between OMNI and IPS observations with $\alpha = -1.0$, $\alpha = 0.0$, and $\alpha = 1.0$. A similar pattern of dV and σ_V variations was revealed for different values of α, and this pattern is almost the same as that shown in Figure 2(a). A distinct change between the different α values was found in the absolute value of dV; the dV shifts to a smaller value as α increases. The large excursion of dV to a positive value after 2009 is suppressed in the CAT analysis with $\alpha = 1.0$, while most of the dV before that drops below zero. The average values of dV for 1985–2008 and 2009–2019 are -22.4 km s^{-1} and 34.6 km s^{-1}, respectively. Table 1 summarizes the average values of dV, σ_V, and correlation coefficients over the analysis period obtained from the IPS-OMNI comparison for the different values of α. The dependence of dV on α is clearly revealed in this table: dV tends to decrease with increasing α, and the best match between IPS and OMNI observations is achieved at $\alpha = 0.5$. The dV for the case $\alpha = 0.5$ is negative (-17.6 km s^{-1}) on average for 1985–2008; the IPS observations systematically underestimate the solar wind speed at 1 au for this period. Unlike dV, σ_V exhibits a weak dependence on α with a minimum value at approximately $\alpha = 1.0$. The correlation coefficients also show a weak dependence on α with a maximum at around $\alpha = 0.0$.

Table 2 lists the average values of dV, σ_V, and the correlation coefficients over the analysis period obtained from the IPS-Ulysses comparison. The systematic change of dV with α is revealed here as the case of the IPS-OMNI comparison;

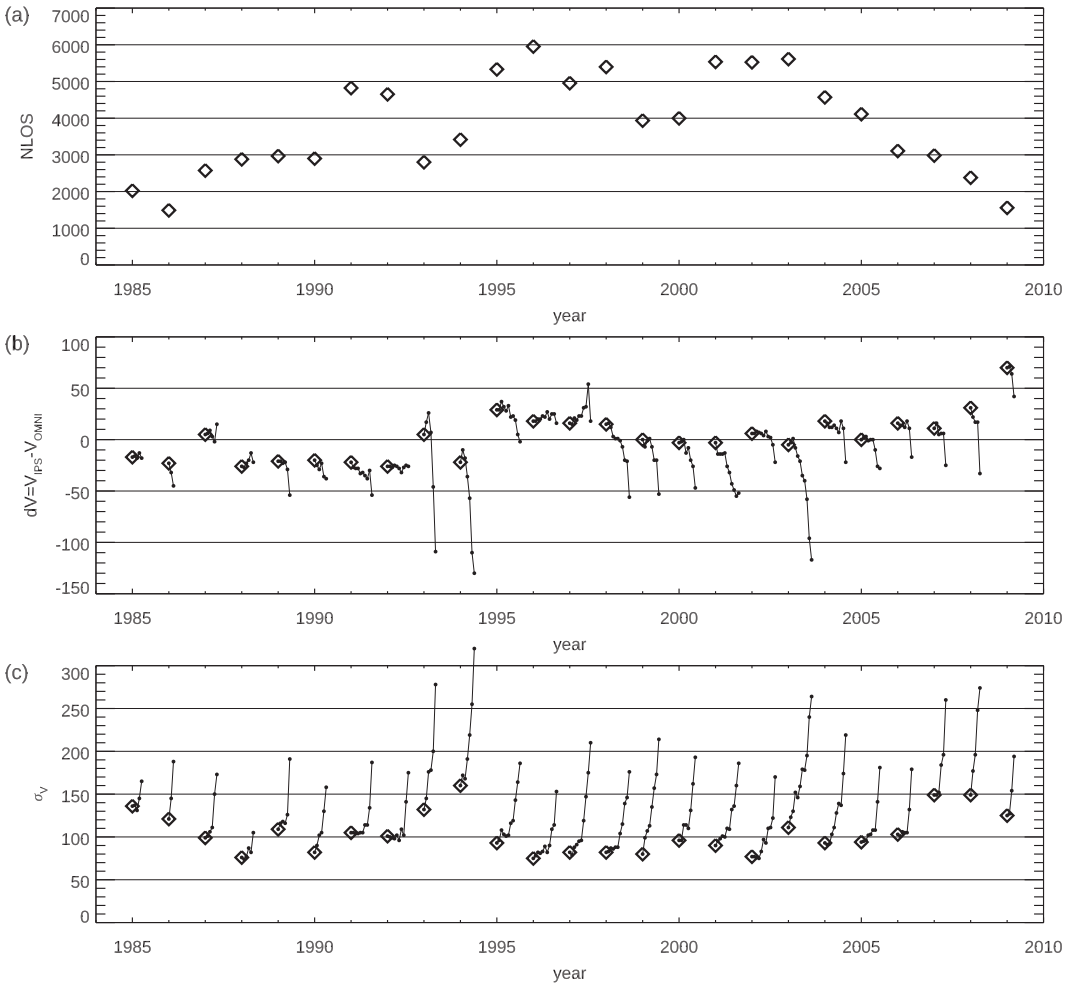

Figure 7. Yearly variation of (a) number of all IPS data, (b) dV, and (c) σ_V between 1985 and 2009. The diamonds for a given year indicate values derived from the CAT analysis using all IPS data, and a solid line connected to the diamond shows the dependence on the reduction of IPS data. The end point of the solid line corresponds to a value derived from the CAT analysis with 500 IPS data.

however, the best match is achieved at $\alpha = -0.5$ in this case. The difference in the best match value of α is ascribed to the fact that Ulysses observations do not include the recent period. As the case of IPS-OMNI comparison, σ_V and the correlation coefficients weakly depend on α, and σ_V becomes the smallest at around $\alpha = -0.5$. The correlation coefficients also indicate that an optimal value of α is between -0.5 and 0.0. These results confirm that the index $\alpha = -0.5$ is optimal for the CAT analysis of the IPS observations taken before 2009.

3.4. CAT Analysis Optimized to In Situ Observations

The CAT analysis is found to be dependent on index α, and this suggests that the discrepancy between IPS and in situ observations after 2009 can be improved by adjusting the value of α. We examined the effect of other parameters used in the CAT analysis such as the angular width of the spread function to blend between adjacent LOS, the minimum number of LOS crossings to yield valid data, and the radial distance range of IPS data for analysis, and did not find any effects to improve the discrepancy. Hence, the index α is an only parameter of the CAT analysis to reconcile discrepancies between IPS and in situ observations after 2009, as far as we know. In this study, we use 15°, 3, and 0.1–1.0 au for the angular width of the spread function, the minimum number of LOS crossing, and the radial distance range, respectively.

If α is changed from -0.5 to a positive value after 2009, the CAT analysis fits OMNI observations better. Therefore, we use $\alpha = 1.0$ as an optimal value for the period after 2009 in this study. The performance of the CAT analysis: dV, σ_V, and correlation coefficients, with optimal index values is shown in Table 3. Figure 9 shows the variation in dV and σ_V derived from the IPS-OMNI comparison. While the increasing trend of dV for the recent period remains in the data from the IPS-OMNI comparison, the average values of dV for the recent (2009–2019) and entire periods are 34.6 ± 23.4 km s^{-1} and 7.5 ± 25.8 km s^{-1}, respectively, and they are smaller than those for $\alpha = -0.5$. This improvement is for dV and hardly for σ_V and the correlations. Thus, an increase in the amount of IPS data is essential to reduce σ_V and improve the correlations. The data from the IPS-Ulysses comparison are almost the same as those for $\alpha = -0.5$.

3.5. Comparison with the Simultaneous Deconvolution Method

In the earlier study (Tokumaru et al. 2012), the relation between ΔN_e and V was investigated using the simultaneous deconvolution method of ISEE IPS observations for the period during 1997–2009, and the best-fit power-law function

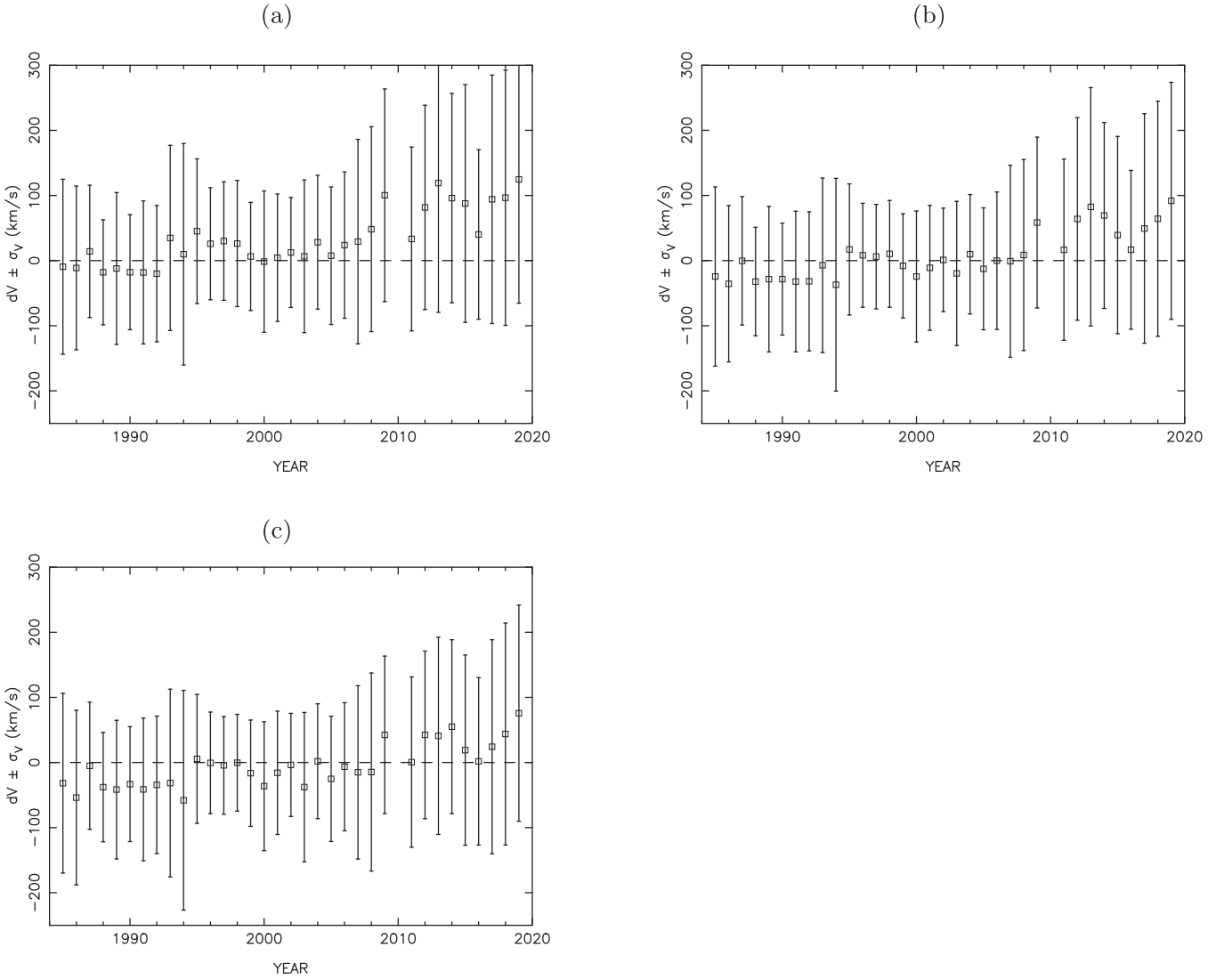

Figure 8. dV (square) with $\pm\,\sigma_V$ (vertical bar) from IPS-OMNI comparison during 1985–2019 for (a) $\alpha = -1.0$, (b) $\alpha = 0.0$, and (c) $\alpha = 1.0$.

Table 1
Averaged Values of dV, σ_V, and Correlation Coefficients (CC) from IPS-OMNI Comparison for Different α

α	dV (km s^{-1})	σ_V (km s^{-1})	CC
(1)	(2)	(3)	(4)
−1.0	32.9 ± 41.0	129.2 ± 36.0	0.307
−0.5	19.1 ± 39.0	124.1 ± 34.6	0.314
0.0	8.2 ± 35.9	120.8 ± 32.6	0.313
0.5	0.2 ± 33.2	118.2 ± 30.1	0.313
1.0	−5.6 ± 32.4	117.1 ± 29.2	0.310
2.0	−11.6 ± 33.0	117.9 ± 27.7	0.289

Table 2
Average Values of dV, σ_V, and Correlation Coefficients (CC) from IPS-Ulysses Comparison for Different α

α	dV (km s^{-1})	σ_V (km s^{-1})	CC
(1)	(2)	(3)	(4)
−1.0	20.6 ± 31.9	105.7 ± 19.5	0.388
−0.5	−2.1 ± 33.1	105.2 ± 22.5	0.383
0.0	−19.5 ± 39.4	109.5 ± 26.8	0.373
0.5	−31.6 ± 44.4	113.0 ± 31.6	0.361
1.0	−39.6 ± 48.4	115.6 ± 35.8	0.354
2.0	−53.9 ± 54.4	125.7 ± 44.1	0.323

$\Delta N_e \propto V^{-0.36\pm0.14}$ was deduced for $V > 350$ km s^{-1}. This result is generally consistent with the power-law index $\alpha = -0.5$ used in the conventional method. We note that observed ΔN_e significantly deviates from this best-fit function to a lower value for $V < 350$ km s^{-1}. This break suggests rarefaction of the very slow solar wind, which is regarded as a peculiar aspect of Cycle 24 (Tokumaru et al. 2018). In this section, we present the analysis of ISEE IPS observations using the simultaneous deconvolution method for the post-2009

Table 3
Averaged Values of dV, σ_V, and Correlation Coefficients (CC) from IPS-OMNI/Ulysses Comparison Using the CAT Analysis with an Optimized Setting for α

In Situ	dV (km s^{-1})	σ_V (km s^{-1})	CC
(1)	(2)	(3)	(4)
OMNI	8.5 ± 25.7	118.3 ± 27.6	0.312
Ulysses	−4.1 ± 31.6	104.7 ± 22.2	0.388

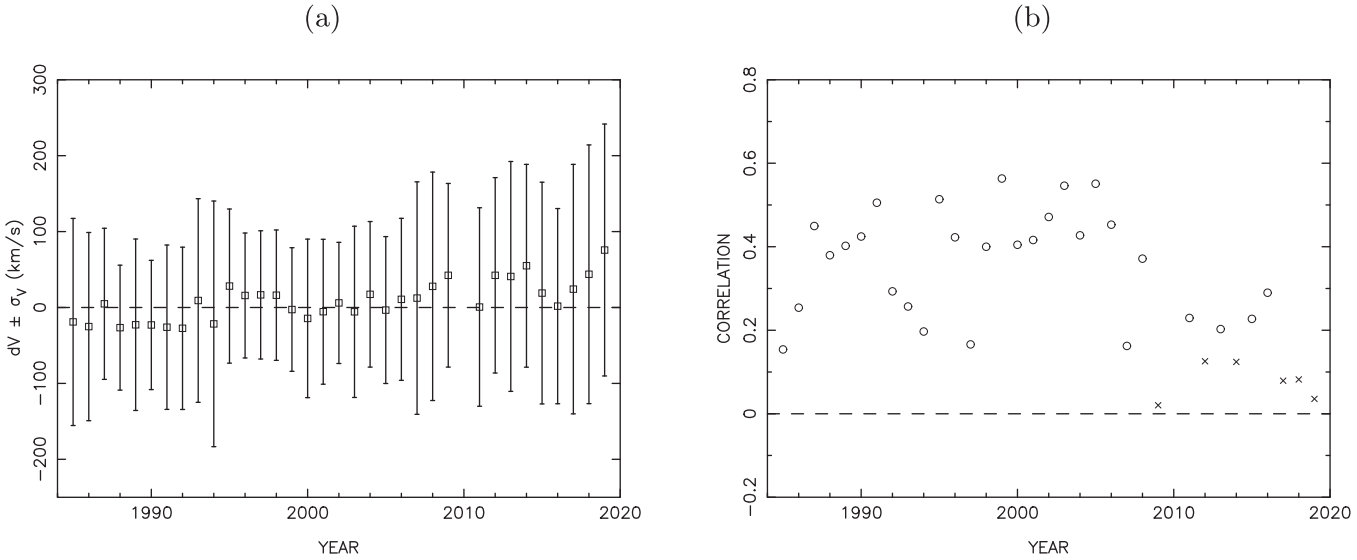

Figure 9. (a) dV (square) with $\pm\ \sigma_V$ (vertical bar), (b) correlation coefficients with $p < 0.05$ (circle) and those with $p > 0.05$ (cross) obtained from IPS-OMNI comparison during 1985–2019 using the CAT analysis with an optimized setting for α.

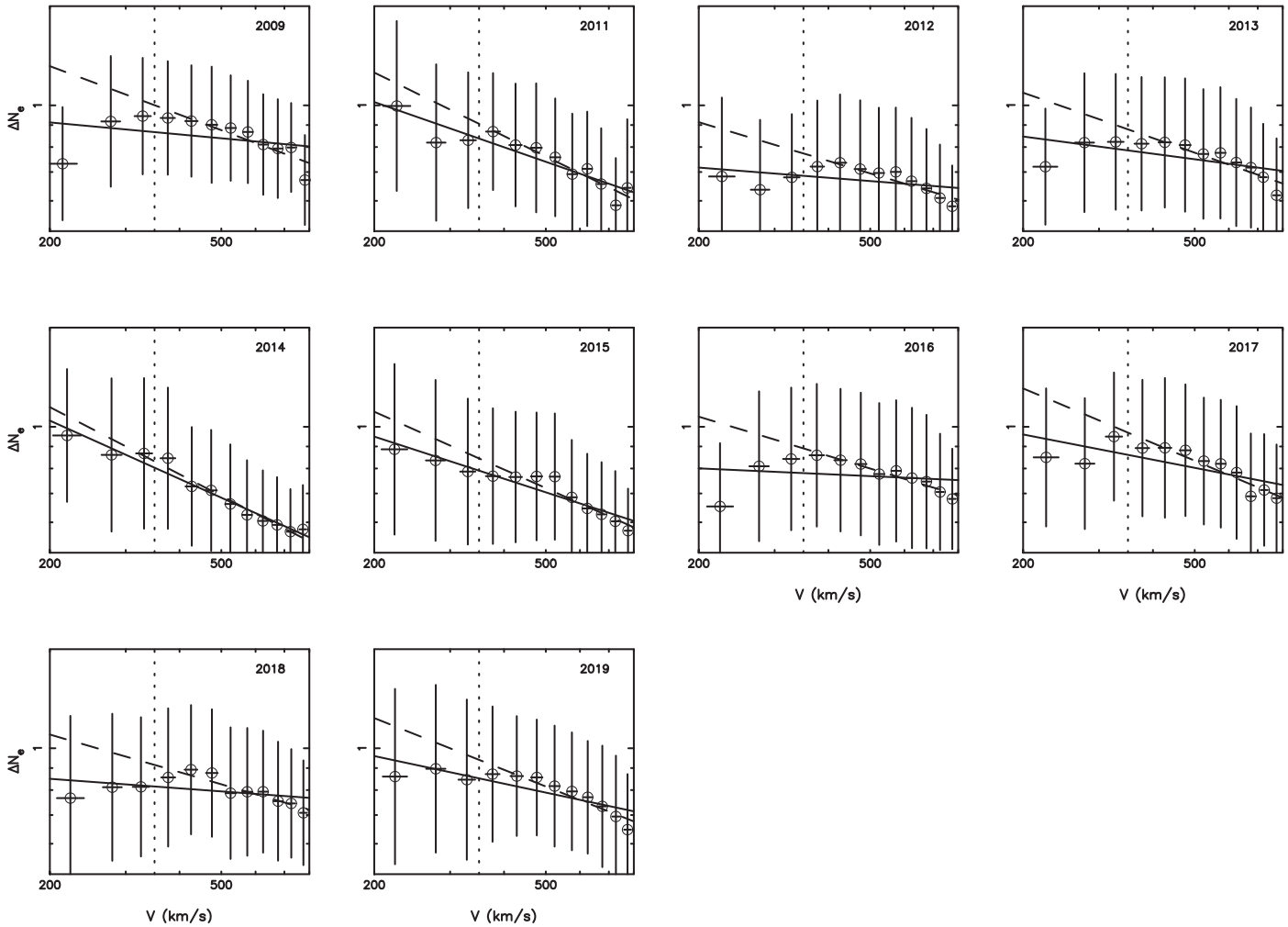

Figure 10. Relation between ΔN_e and V plotted in the log–log format for each year between (top left) 2009 and (bottom right) 2019. Note that no data are available for 2010. Solid and dashed oblique lines are the best-fit power-law functions for all V and $V > 350$ km s^{-1} (dotted vertical line), respectively.

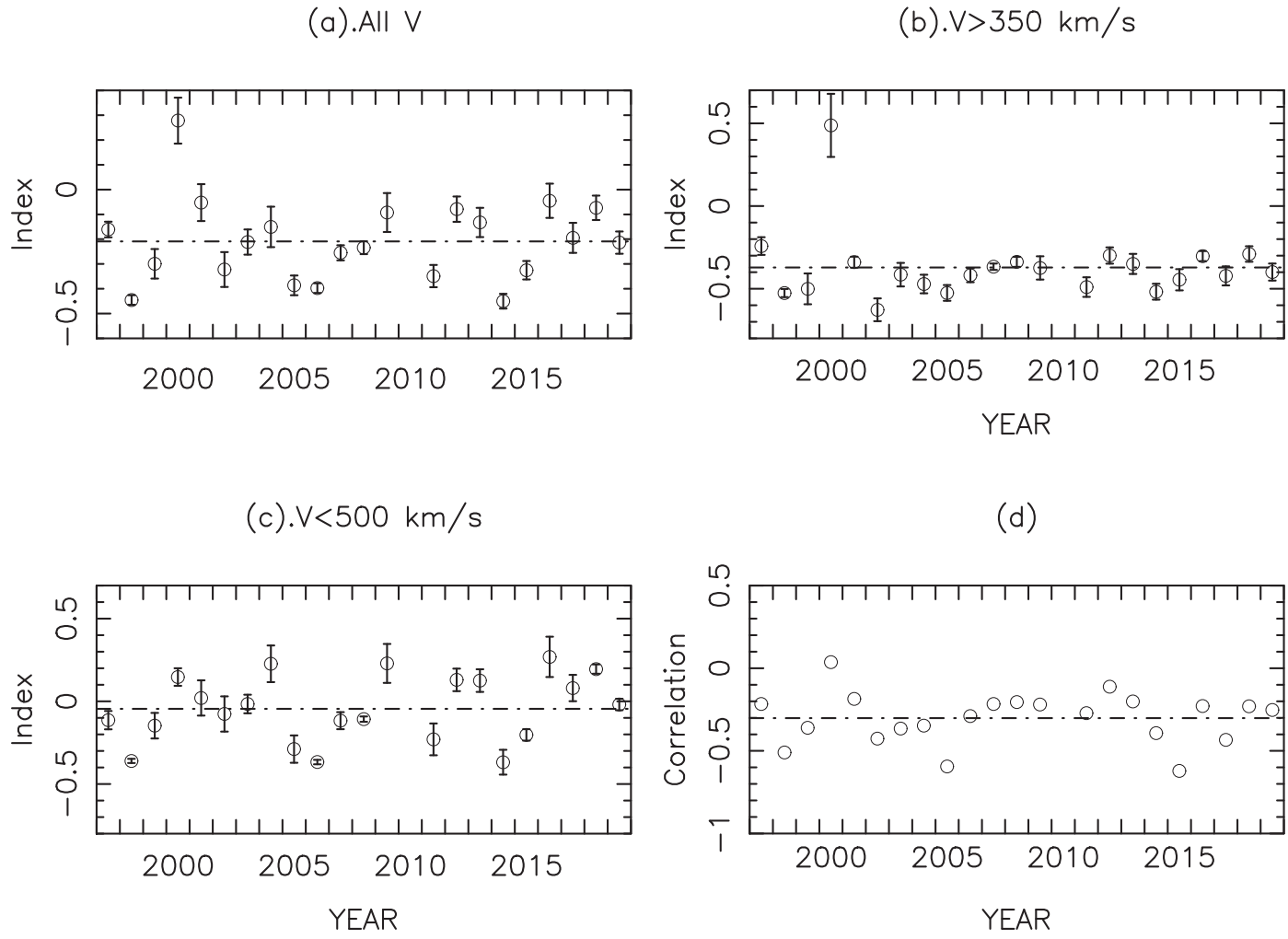

Figure 11. Time variations of the best-fit power-law indices for (a) all V, (b) $V > 350$ km s^{-1} and (c) $V < 500$ km s^{-1}, and (d) the correlation coefficients between ΔN_e and V during 1997–2019. A horizontal dashed–dotted line in each plot shows the average value.

period. To investigate the ΔN_e–V relation, ΔN_e data were compared with V data on a pixel-by-pixel basis of the source surface map. Figure 10 shows dependence of ΔN_e on V for each year between 2009 and 2019. This figure is basically the same as Figure 10 of Tokumaru et al. (2012) but for the period. Solid and dashed lines in the figure represent power-law functions fit for all V and $V > 350$ km s^{-1}, respectively. As shown in the figure, ΔN_e is inversely correlated with V for $V > 350$ km s^{-1}, and this variation is explained by the best-fit power-law function with a negative index. Further, ΔN_e for $V < 350$ km s^{-1} tends to drop below the best-fit function. The drop in ΔN_e for $V < 350$ km s^{-1} results in flatter indices of the power-law function fit for all V. These features are quite similar to what was revealed from Tokumaru et al. (2012).

The power-law indices of the best-fit function $\Delta N_e \propto V^x$ determined on a yearly basis for all V and $V > 350$ km s^{-1} are plotted as a function of the year in Figures 11(a) and (b), respectively. The correlation coefficients between ΔN_e and V calculated on a pixel-by-pixel basis of the source surface map are plotted in Figure 11(d). These plots include data for the period between 1997 and 2019. The power-law indices for all V are systematically flatter than those for $V > 350$ km s^{-1}, and the average values are -0.21 ± 0.16 and -0.37 ± 0.21 for all V and $V > 350$ km s^{-1}, respectively. A large excursion of data for 2000 is likely due to the effect of the rapid evolution of the solar wind distribution at solar maximum (Tokumaru et al. 2012). Weak negative correlations are revealed for most of the analysis years, and the average value is -0.30 ± 0.15. These correlations are statistically significant because the p-values are sufficiently small. The important point to note is that no long-term trend is clearly discernible in the indices, and this appears inconsistent with what we argued in the previous section. The average values of the indices for all V are -0.23 ± 0.19 for 1997–2008 (Cycle 23) and -0.20 ± 0.14 for 2009–2019 (Cycle 24), and the former is slightly flatter than the latter, while the difference is well within the rms deviation. When we compare the indices of all V for the Cycle 24/25 minimum (2016–2019) with those for the Cycle 23/24 minimum (2006–2009), the difference becomes slightly more distinct; however, the indices remain negative; the average values of the indices for the Cycle 23/24 and Cycle 24/25 minima are -0.24 ± 0.12 and -0.18 ± 0.08, respectively. This difference may be ascribed to the effect of growth of the low-ΔN_e slow solar wind (Tokumaru et al. 2018). The correlation coefficients also show no long-term change; the average value of the correlation coefficients for Cycle 24 is nearly equal to that for Cycle 23.

Another important point to note is that the solar wind speeds derived from the simultaneous deconvolution method for 2009–2019 show a discrepancy to in situ observations, which is

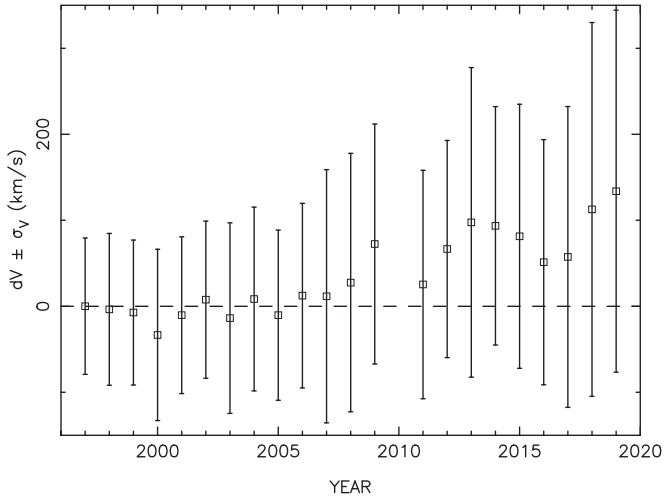

Figure 12. dV (square) with σ_V (vertical bar) from IPS-OMNI comparison using the simultaneous deconvolution method during 1997–2019.

similar to that found from the comparison between IPS and in situ observations using the conventional method. Figure 12 shows the time variation of dV and σ_V calculated from IPS-OMNI comparison using the simultaneous deconvolution method for 1997–2019. A sudden increase in dV after 2009 is clearly revealed in the figure; the average values of dV are -0.9 ± 16 km s^{-1} for 1997–2008, 79 $\pm$ 32 km s^{-1} for 2009–2019, and 36 $\pm$ 46 km s^{-1} for 1997–2019. These values are similar to those obtained from IPS-OMNI comparison using the conventional method with $\alpha = -0.5$ (Section 3.1). This is consistent with the power-law indices deduced from the simultaneous deconvolution method, which are close to $\alpha = -0.5$.

The indices derived from the simultaneous deconvolution method show negative values close to $\alpha = -0.5$ even for the recent period, and thus the discrepancy between IPS and in situ observations cannot be improved. To use a positive value (e.g., $\alpha = 1.0$) as the index is the only way to improve the discrepancy between IPS and in situ observations, as far as we know. We consider that the current version of the simultaneous deconvolution method does not properly retrieve the relation between ΔN_e and V. Although the cause for this problem is not fully understood yet, one possibility is that the relation between ΔN_e and V has a complex feature in the recent period. Figure 13 shows 2D plots of ΔN_e and V data derived from the simultaneous deconvolution method for 2009–2019. As revealed in the figure, IPS data are composed of two groups: that broadly distributed around $\Delta N_e \sim 1$ and that sharply distributed at $\Delta N_e < 0.5$. The broad distribution group appears consistent with the inverse relation between ΔN_e and V. On the other hand, the sharp distribution group do not show a clear dependence on V. The latter group may be linked to the low ΔN_e slow solar wind which becomes prominent in the recent period, although it includes data with a wide range of V. The property of solar wind microturbulence in the recent period is considered to evolve in a complex way owing to the sharp distribution group associated with low ΔN_e. This may cause the failure in retrieval of the actual ΔN_e–V relation from the simultaneous deconvolution method. Hence, we consider that the conventional method with different values for α depending on the period is presently the best option to address the global distribution of the solar wind speed from IPS observations.

Figure 10 suggests that the break point speed of the ΔN_e–V relation increased with the growth of the low-ΔN_e slow solar wind, being as high as 500 km s^{-1} in the recent period. The slow solar wind, whose typical speed is lower than this, is considered to be entirely included in the low-ΔN_e group for the recent period. The best-fit functions $\Delta N_e \propto V^{\alpha}$ for $V < 500$ km s^{-1} are plotted in Figure 13 (dashed line), and the time variation of α for $V < 500$ km s^{-1} during 1997–2019 is shown in Figure 11(c). The indices α for $V < 500$ km s^{-1} are much flatter than those for all V, and positive slopes are observed for several years. The occurrence of positive slopes appears to increase after 2009, and this may reflect the growth of the low-ΔN_e slow solar wind. As the break point speed increases, the index α of the slow solar wind is expected to change from negative to positive values. The OMNI-IPS comparison is likely to be significantly affected by this change because the heliosphere in the ecliptic plane where OMNI observations were made is dominated by the slow solar wind. Therefore, the result of the simultaneous deconvolution method may be qualitatively consistent with the argument in the previous section.

4. Solar Cycle Variation of Solar Wind Speed Distribution

Figure 14 shows a synoptic source surface map of the solar wind speed derived from our IPS observations between 1985 and 2019. This map was produced from the CAT analysis with an optimal setting for α. Multi-station IPS observations are interrupted every winter owing to snow, and they are interrupted irregularly owing to system maintenance and replacement with a new system. Despite these interruptions, the solar cycle variation of the solar wind speed distribution is clearly shown in this figure. The solar wind speed distribution changes systematically with the solar cycle, and the most distinct change in the solar wind speed distribution occurs at the poles of the Sun. The fast solar wind (blue area) develops at high to mid latitudes during four periods around 1985, 1996, 2008, and 2019, which correspond to the Cycle 21/22, 22/23, 23/24, and 24/25 minima, respectively. It almost disappears in the solar maximum periods around 1990 (Cycle 22), 2000 (Cycle 23), and 2014 (Cycle 24). The slow solar wind (red area) dominated all latitudes during the solar maximum periods. In contrast to the poles, the equatorial region is always associated with slow solar wind, regardless of the solar cycle phase.

4.1. Relationship between the Solar Wind Speed Distribution and the Polar Magnetic Field Strength

The IPS data of the three cycles display a similar pattern of solar cycle variation; however, there are some distinct differences between them. To examine the solar cycle variation of the solar wind speed distribution in more detail, we calculated the fractional area for fast (>700 km s^{-1}), slow (<445 km s^{-1}), and intermediate speed ranges on a yearly basis. The fractional area is given by the ratio of the source surface area associated with a given speed range to that of the region where the IPS observations are available. The intermediate speed ranges are divided into three groups in terms of speed with an equal range width: 445–530, 530–615, and 615–700 km s^{-1}. The annual variation of the fractional areas for different speed ranges during 1985–2019 is shown in

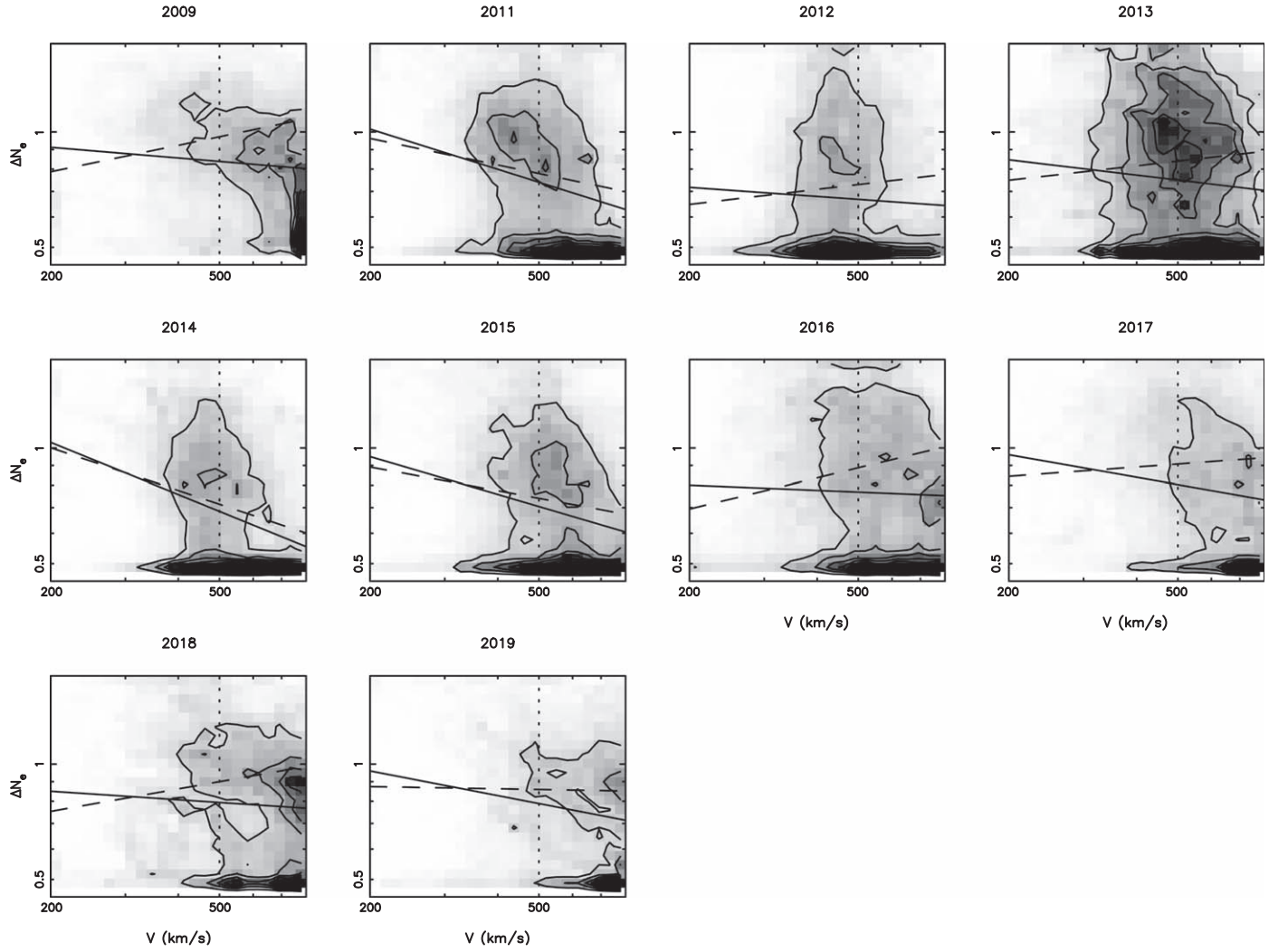

Figure 13. ΔN_e vs. V maps produced on a yearly basis during 2009–2019. The contours and gray shades represent the occurrence rate of data. Solid and dashed oblique lines are the best-fit power-law functions for all V and $V < 500$ km s^{-1} (dotted vertical line), respectively.

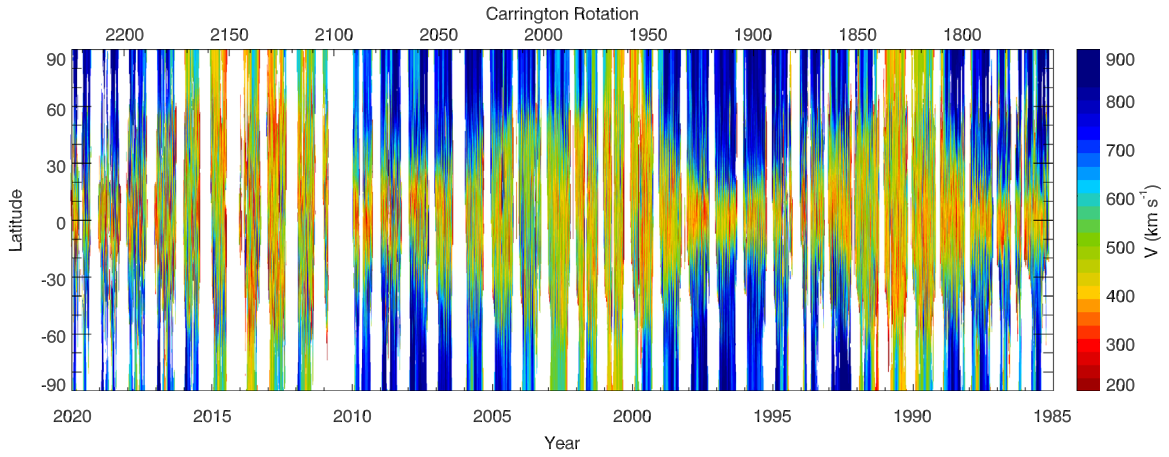

Figure 14. Synoptic source surface map of the solar wind speed derived from IPS observations during 1985–2019. The Carrington rotation number; i.e., the time increases from the right to the left in this map.

Figure 15(c). In this figure, the variations in the sunspot numbers (panel (a)) and the polar field strength derived from magnetograph observations at WSO (panel (b), Svalgaard et al. 1978; Hoeksema 1995) are also indicated. The sunspot number and polar field data are obtained from http://www.sidc.be/silso/datafiles and http://wso.stanford.edu/Polar.html, respectively. This figure clearly demonstrates that the alternative growth and decline of fast and slow winds are strongly

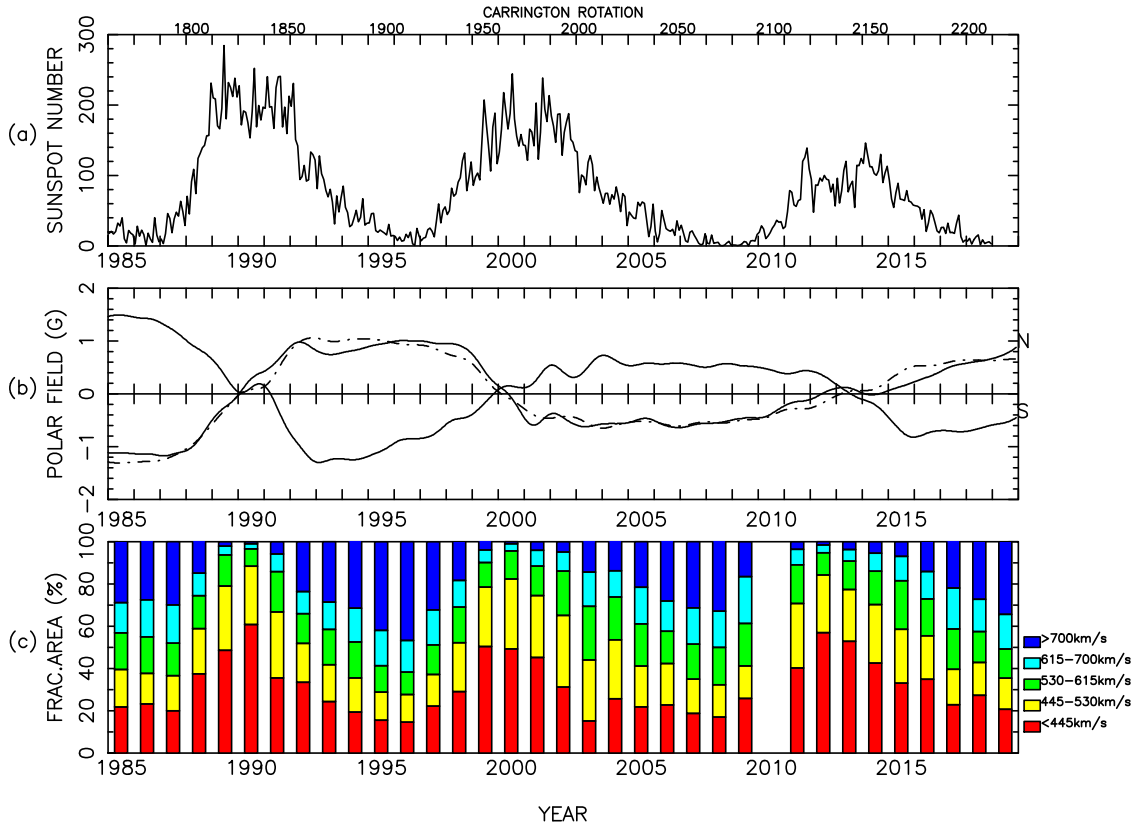

Figure 15. Time variations of (a) sunspot numbers, (b) polar field strength derived from magnetograph observations at WSO, and (c) fractional source surface areas for different solar wind speed ranges during 1985–2019. In the middle panel, two solid lines indicate data at north (N) and south (S) poles, and the dashed–dotted line indicates the average value (N–S)/2. In the bottom panel, red, yellow, green, cyan, and blue bars correspond to <445, 445–530, 530–615, 615–700, and >700 km s^{-1}, respectively.

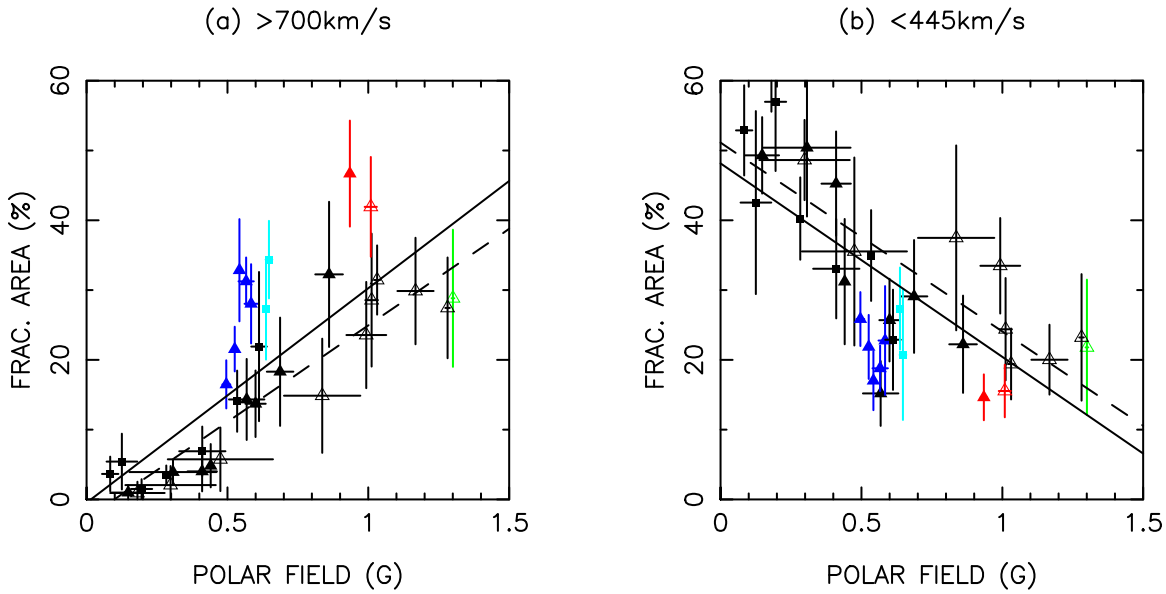

Figure 16. Correlation diagrams between the yearly mean polar field strength and fractional area (a) >700 km s^{-1} and (b) <445 km s^{-1}. Open, filled triangles and filled squares represent data taken during Cycles 22 (1985–1995), 23 (1996–2008), and 24 (2009–2019), respectively. Green, red, blue, and cyan correspond to data at the Cycle 21/22, 22/23, 23/24, and 24/25 minima, respectively. Solid and broken oblique lines indicate linear regression lines for all data and those excluding minimum data, respectively.

correlated with the change in sunspot numbers and polar field strengths.

Figure 16 shows correlation between polar fields and fast wind areas (panel (a)), and that between polar fields and slow wind areas (panel (b)). The polar field data are averaged over every year to compare fractional area data. The fast wind areas have a positive correlation with polar fields, and slow wind areas have a negative correlation, as shown in Figure 16. The correlation coefficients between fractional areas and polar fields are 0.80 and −0.72 for fast and slow winds, respectively. These

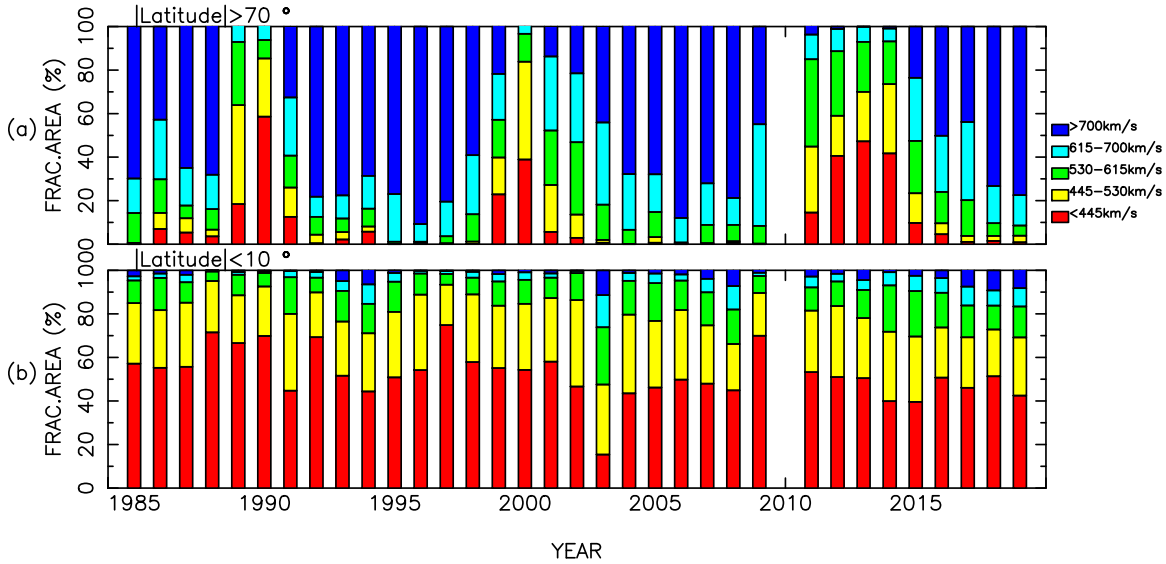

Figure 17. Time variations of fractional area data taken at (a) high latitudes, and (b) low latitudes during 1985–2019. Color represents the solar wind speed.

results are explained by the growth and decay of polar coronal holes over the course of the solar cycle. The variations of fast and slow wind data at the Cycle 24/25 minimum are similar to those at the Cycle 23/24 minimum, being commensurate with the weak polar fields at both minima. The interesting point is that fast (slow) winds tend to be formed at solar minima more (less) than those expected from the linear regression line (solid lines), although this is not the case for the Cycle 21/22 minimum, i.e., 1985. If we exclude data for 1995–1996, 2005–2009, and 2018–2019, we obtain better correlation coefficients: 0.92 for fast winds and −0.78 for slow winds, respectively. This fact may be ascribed to the effect of the quadrupole moment of the Sun's magnetic field (Tokumaru et al. 2015).

4.2. Latitude Dependence of the Solar Wind Speed Distribution

Figure 17 illustrates the latitude dependence of the solar wind speed distribution. Panels (a) and (b) show the fractional area data for high and low latitudes, respectively. The high-latitude region is dominated by fast winds, except for a few years around the solar maxima. There are two distinct points in the high-latitude data of Cycle 24. First, the period when high-latitude fast winds disappear at the Cycle 24 maximum is longer than those at the Cycle 22 and 23 maxima. Second, a broad peak of slow wind areas was observed at the Cycle 24 maximum. This peak is associated with the double-peak feature found in the sunspot number variation (see Figure 11(a)) and north–south asymmetry of the polar solar wind at the Cycle 24 maximum (see the next subsection). In contrast, the low-latitude region is dominated by slow winds. At low latitudes, slow (<445 km s^{-1}) wind areas are almost constant, whereas they appear to slightly decrease in the period between Cycles 22 and 23. The average values of the slow wind fractional area for Cycles 22, 23, and 24 are 58% ± 10%, 50% ± 13%, and 49% ± 9%, respectively. The difference between Cycles 22 and 23 is insignificant because it is within the rms deviation. The fast (>700 km s^{-1}) wind areas at low latitudes are a negligible fraction throughout the analysis period, and the average value is 3% ± 3% for 1985–2019. The fast wind areas appear to increase by 5% in the Cycle 24/25 minimum: the average value for 2017–2019 is 8% ± 1%. However, we cannot safely say that this change is an intrinsic one, because the tendency for IPS observations to be higher than those from in situ (OMNI) observations remains in the improved CAT analysis for the recent period, as mentioned in Section 3.4.

Figure 18 shows the comparison of fractional area data between four solar minima: 1985 (Cycle 21/22), 1996 (Cycle 22/23), 2008 (Cycle 23/24), and 2019 (Cycle 24/25). Fractional area data taken at solar minima show a common feature: dominance of the fast wind at high (even all) latitudes and that of the slow wind at low latitudes. Nevertheless, we find differences between the data at four minima. The fast wind area of 2019 for all latitudes (panel (a)) is nearly the same as those of 2008 and 1985 (33% and 29%, respectively); however, it is significantly smaller than that of 1996 (47%). The fast wind areas for high latitudes (panel (b)) have a similar tendency. Fractional area data of other speed ranges do not clearly show such a tendency, while a less distinct inverse trend is observed for the data of 530–615 km s^{-1} at all latitudes and those of 615–700 km s^{-1} at high latitudes. In contrast, at low latitudes (panel (c)), the slow wind areas of 2008 and 2019 (45% and 42%, respectively) is significantly smaller than those of 1985 and 1996 (57% and 54%, respectively), thereby showing a similarity. The fast wind areas of 2008 and 2019 at low latitudes (7% and 8%, respectively) were larger than those for 1985 and 1996 (3% and 0.2%, respectively). However, the CAT analysis tends to overestimate the solar wind speed in the recent period (see Section 3.4); therefore, we cannot rule out the possibility that data in 2019 are biased by this effect

4.3. North–South Asymmetry of Polar Solar Wind

We calculated the average speed over regions at |latitude| >70° using IPS observations. Figure 19 shows the variations of the average speeds over the north and south poles and the difference V_{N-S} between the north and south poles during 1985–2019. A positive value of V_{N-S} corresponds to an excess of the north pole speed. Fast solar winds are observed over the poles except for short periods around the solar maxima when the polar solar wind speeds become slow. The difference V_{N-S} is usually small, within ±50 km s^{-1}; however, it develops

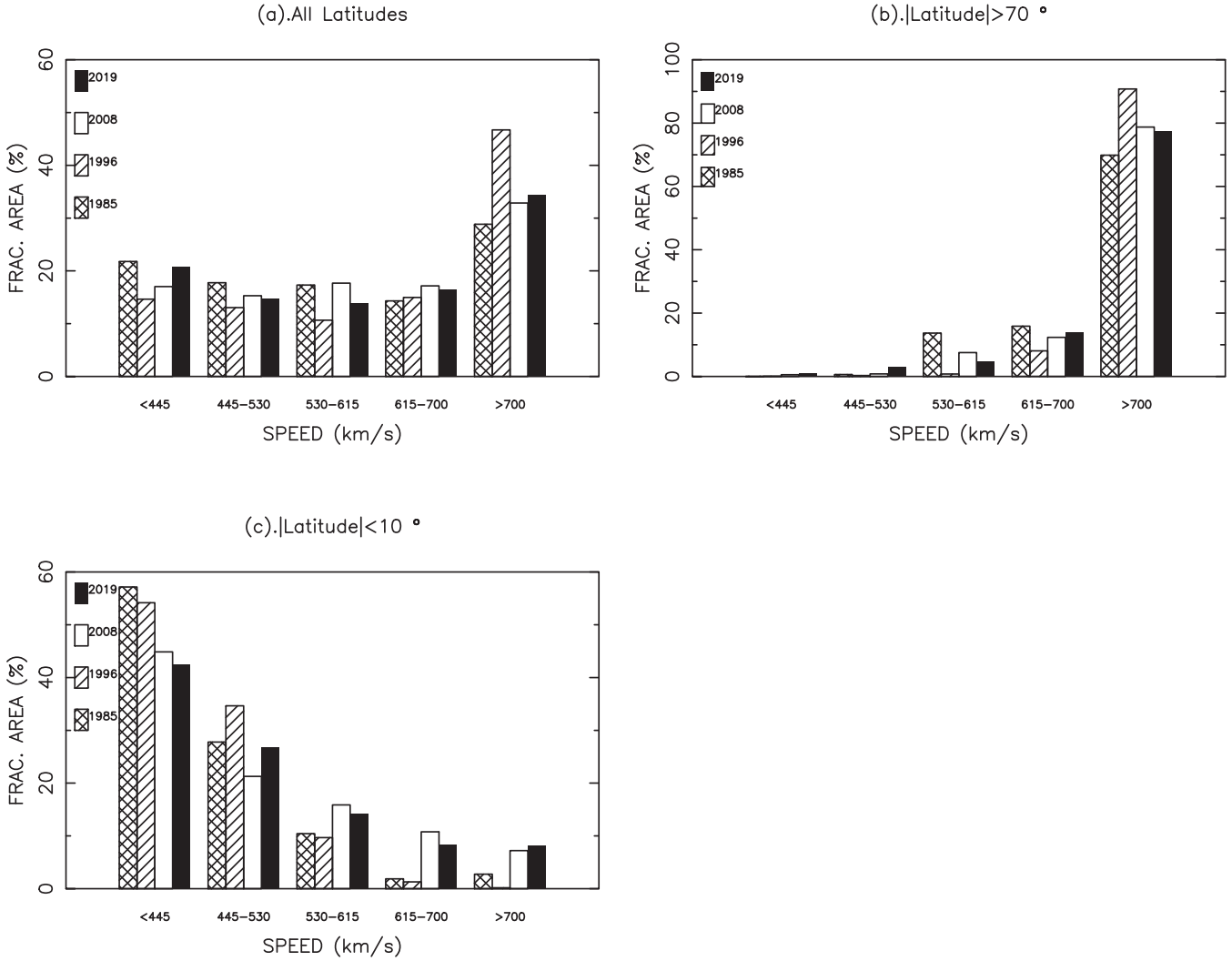

Figure 18. Comparison of fractional areas taken at (a) all latitudes, (b) high latitudes, and (c) low latitudes for solar minimum years 1985, 1996, 2008, and 2019.

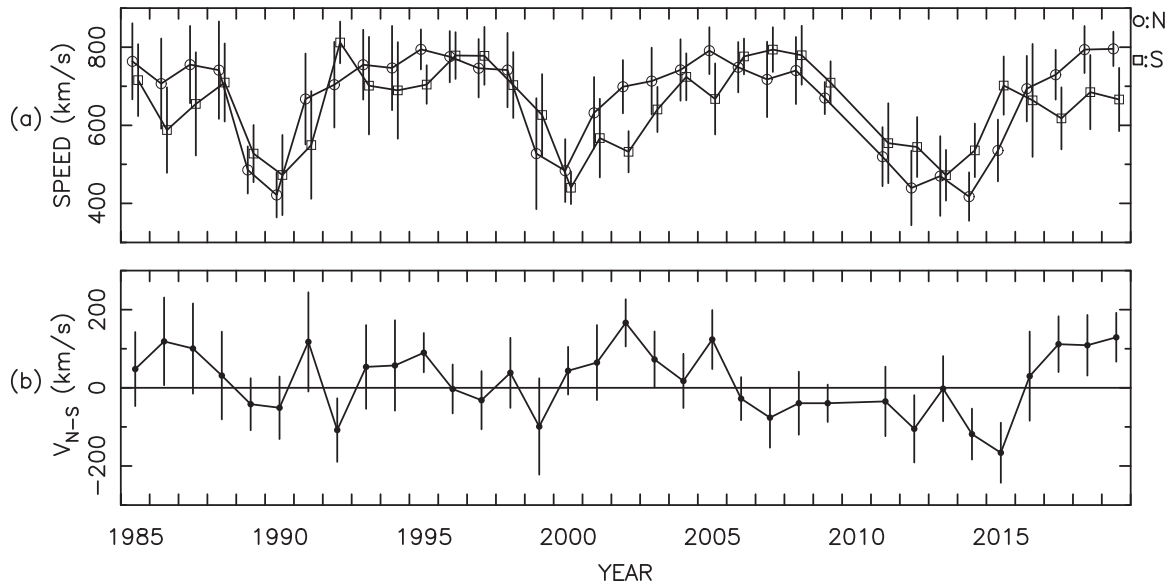

Figure 19. Time variations of (a) the solar wind speeds averaged over north (circle) and south poles (square), and (b) difference between averaged speeds V_{N-S} over north and south poles.

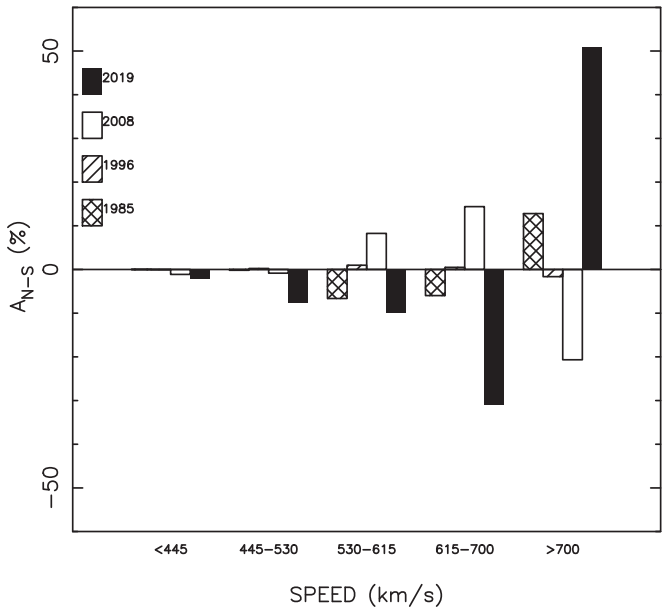

Figure 20. Comparison of differences between fractional areas A_{N-S} over north and south poles for 1985, 1996, 2008, and 2019.

during the solar maxima. The timing of the transition from fast to slow winds was significantly different between the north and south poles. The solar wind speed over the north pole drops earlier than that over the south pole at the Cycle 22, 23, and 24 maxima, and this results in the occurrence of the north–south asymmetry in the solar wind speed over the poles, as reported in our earlier paper (Tokumaru et al. 2015). The fast wind over the north pole reappears earlier than that over the south pole at the Cycle 22 and 23 maxima. The reappearance of the polar fast winds at the Cycle 24 maximum is different from those at the Cycle 22 and 23 maxima; the solar wind speed over the north pole increased in 2013, but fell in 2014, and rose again in 2015, whereas the solar wind speed over the south pole increased in 2014, reaching ∼800 km s^{-1} earlier than that over the north pole. The solar wind speed over the south pole dropped from ∼800 to ∼700 km s^{-1} in 2017, and remained at this level until 2019. Therefore, the polar solar wind of Cycle 24 maintains north–south asymmetry in speed even after the reappearance of the fast wind after the maximum.

Figure 20 shows a comparison of north–south asymmetry of the polar solar wind between four solar minima: 1985, 1996, 2008, and 2019. In this figure, the difference between fractional areas of northern and southern high-latitude regions with |latitude| >70°, A_{N-S} are plotted, and a positive value of A_{N-S} corresponds to an excess of the northern fractional area. A marked enhancement of A_{N-S} is observed for 2019 (Cycle 24/25 minimum) at speed ranges >700 and 615–700 km s^{-1}, which correspond to excesses of northern and southern area, respectively. This is consistent with the decrease in the mean wind speed over the south pole mentioned above. Another enhancement of A_{N-S}, which is about a half of that of 2019, is observed for 2008 (Cycle 23/24 minimum) at >700 and 615–700 km s^{-1}. Interestingly, the signs of enhanced A_{N-S} at these ranges are inverted as compared to those for 2019. For 1985 and 1996, the magnitude of A_{N-S} never exceeds 13%, close to zero at all speed ranges, suggesting that the north–south asymmetry is insignificant at the Cycle 21/22 and 22/23 solar minima. Therefore, the development of the north–south asymmetry of the polar solar wind is a peculiar aspect of the Cycle 24 minima.

5. Comparison with PSP Observations

Figure 21 shows the comparison of IPS and PSP observations for the period around the perihelion of Orbit 1, which occurred on 2018 November 6. This period corresponds to Carrington rotation (CR) 2210. The locations of PSP observations are projected back to the source surface at 2.5 R_S under the assumption that the solar wind flows radially at a constant speed measured by PSP. As shown in the figure, PSP observations covers a short period in the early part of CR 2210 and the middle of CR 2211. In the period of CR 2211, which corresponds to late November to December 2018, IPS observations are considerably few owing to interruptions during winter. Therefore, a meaningful comparison between IPS and PSP observations is available only for the early part of CR 2210. During this period, the solar wind speeds measured by PSP rises from ∼300 to ∼550 km s^{-1}, then falls to ∼400 km s^{-1}. The IPS observations also show similar rise and fall in the solar wind speed, whereas the peak speed measured by IPS is somewhat smaller than that by PSP by a factor of 0.9. Variation of IPS observations is rather smooth, compared to that for PSP observations. This is ascribed to a limited spatial resolution of the CAT analysis, and an increase in the number of LOS is essential for improving the spatial resolution. Nevertheless, IPS observations mostly agree with PSP observations for the period of Orbit 1 perihelion, and this is regarded as an evidence to support the reliability and validity of the CAT analysis of IPS observations.

Figure 22 shows a correlation diagram between IPS and PSP observations. The correlation coefficient between them is 0.68. We calculate dV and σ_V from the IPS-PSP comparison, and we obtain $dV = -23.0$ km s^{-1} and $\sigma_V = 71.9$ km s^{-1}. IPS observations slightly underestimate in situ measurements by PSP. While the magnitude of this discrepancy is comparable to the estimation error of the CAT analysis, it is in the opposite sense to that found from the IPS-OMNI comparison. If this discrepancy is intrinsic, it may suggest that the solar wind decelerates during propagation between the PSP orbit (∼35 R_S) and larger distances where IPS observations were taken. Owing to the limited amount of data available here, we cannot say for certain whether this discrepancy is intrinsic or not. We will defer further discussions on radial evolution of the solar wind speed to a future study using PSP and IPS observations more extensively.

6. Summary and Discussion

We compared the solar wind speed data derived from the CAT analysis of IPS observations with those from OMNI and Ulysses in situ observations between 1985 and 2019. We found that the solar wind speeds derived from IPS observations are in agreement with those from the in situ observations for the period until 2008; however, they tend to be higher than those after 2009. Further, we found that the rms deviations and correlation coefficients between IPS and in situ observations increased and decreased, respectively, in the recent period. These changes in rms deviations and correlation coefficients are attributed to the effect of reduced LOS for IPS observations, whereas the tendency for IPS observations to overestimate the solar wind speed cannot be explained by the effect of reduced

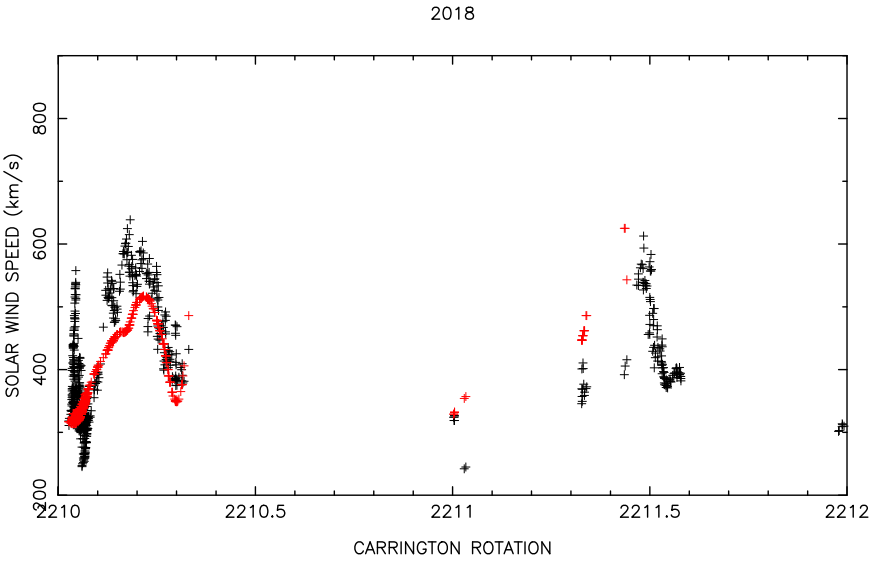

Figure 21. Time variations of the solar wind speeds obtained from IPS observations (red) and PSP in situ observations (black) at around the perihelion of Orbit 1.

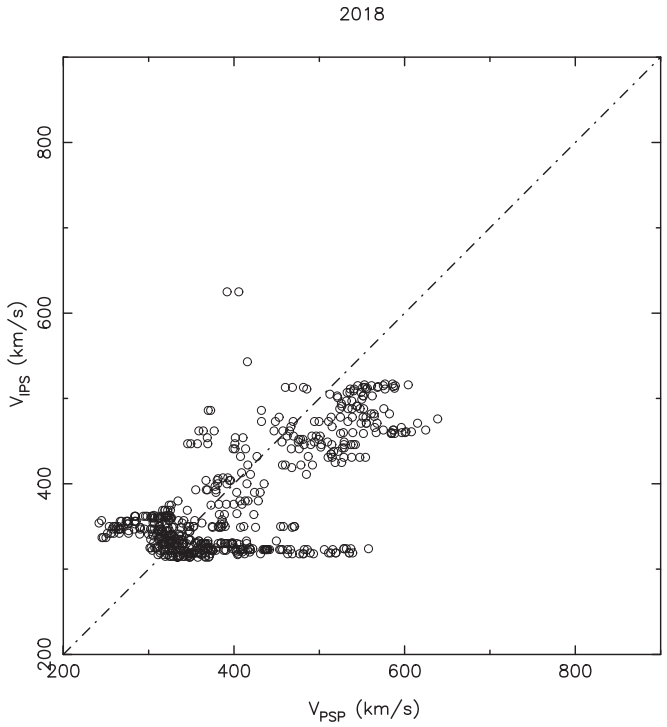

Figure 22. Comparison between solar wind speeds from PSP V_{PSP} and IPS observations V_{IPS}.

LOS. We found that the discrepancy between IPS and in situ observations for the recent period was improved by changing the index α. The CAT analysis with $\alpha = -0.5$ yielded the best performance in analyzing IPS observations for 1985–2008. We found that $\alpha = 1.0$ was optimal for the CAT analysis in the recent period: 2009–2019. Although the optimal setting for α reduced the discrepancies between IPS and in situ observations, the tendency for IPS to overestimate the solar wind speed still remains. Therefore, further improvement of the CAT analysis, which is left for future work, is needed.

The empirical relationship $\Delta N_e \propto V^{\alpha}$ can be converted to the relation between the fractional density fluctuations $\Delta N_e/N$ and V by assuming that physical quantities such as mass, momentum, or energy fluxes are uniform among different speed flows: $NV^{\beta} =$ constant (Neugebauer 1992; Le Chat et al. 2012). Earlier studies suggest that the momentum flux ($\beta = 2$) is likely to be invariant (Richardson & Wang 1999; McComas et al. 2008), although this is still an open question. The results of this study suggest that the optimal value of α for the CAT analysis of IPS observations is -0.5 for 1985–2008, and 1.0 for 2009–2019. This means that the speed dependence of solar wind microturbulence may evolve with long-term changes in the large-scale magnetic field of the Sun. If $\beta = 2$, which corresponds to the invariance of the momentum flux, $\alpha = -0.5$ and 1.0 correspond to $\Delta N_e/N = V^{+1.5}$ and V^{+3}, respectively, which suggest $\Delta N_e/N$ becomes more dependent on V in Cycle 24 than in Cycles 22 and 23. Since the efficiency of solar wind acceleration may depend on $\Delta N_e/N$, the results obtained here imply that the acceleration efficiency may vary with the long-term change of the solar cycle.

Using CAT analysis with the optimal setting for α, we determined the global distribution of the solar wind speed from IPS observations between 1985 and 2019. The results revealed that the solar wind speed distribution varied systematically with the solar cycle. The fractional areas of fast and slow winds were found to be highly correlated with the polar field strengths of the Sun, while fast (slow) winds tended to form at solar minima more (less) than the linear regression line. A similar distribution of the solar wind speed is observed at solar minima: fast and slow winds prevail at high and low latitudes, respectively. Some significant differences were found between the four solar minima in the analysis period: the fast wind areas at Cycle 24/25 minimum were similar to those at Cycle 23/24 and 21/22 minima; however, it is significantly smaller than that at Cycle 22/23 minimum. The slow wind areas of Cycle 24/25 and 23/24 minima at low latitudes are similar, but they are smaller than those of Cycle 22/23 and 21/22 minima. Our IPS observations demonstrate that polar solar winds become asymmetric at solar maxima. A distinct north–south asymmetry was found to occur at Cycle 24 maximum and even at Cycle 24/25 minimum, and this is a noticeable point on the Cycle 24 solar wind. The solar wind speed distribution is closely associated with the global structure of the coronal magnetic

field. The solar wind speed is known to be inversely correlated with the magnetic flux expansion factor (Wang & Sheeley 1990; Hakamada & Kojima 1999), and positively correlated with the area of the coronal hole, i.e., the open field region on the photosphere (Nolte et al. 1976; Tokumaru et al. 2017). Our IPS observations demonstrated that the polar solar winds of Cycle 24 are highly asymmetric even at the Cycle 24/25 minimum. Such an asymmetric feature is expected to be observed for the coronal magnetic field, and further discussions are deferred to a future study.

We compared the solar wind speed data derived from IPS observations with those from PSP observations collected around the perihelion of Orbit 1. This result proves that the CAT analysis of IPS observations accurately retrieves the solar wind speed distribution. As mentioned above, the speed dependence of solar wind density fluctuations may change in association with long-term variations in the solar activity, and this is regarded as an important clue to gain insight into the generation mechanism of solar wind microturbulence. While solar wind microturbulence is considered to play an important role in heating and accelerating the solar wind, its physical properties remain unclear owing to shortage of observational data. High cadence in situ measurements of the solar wind with recent spacecraft such as PSP and Solar Orbiter (Müller et al. 2020) allow access to the physics of solar wind microturbulence. A comparison between IPS and these in situ observations will be an interesting future subject, as it will help clarify the relationship between microturbulence properties and solar wind acceleration.

The IPS observations were conducted under the solar wind program of the Solar-Terrestrial Environment Laboratory (STEL), currently the Institute for Space-Earth Environmental Research (ISEE). IPS data are available from the ISEE ftp server (http://stsw1.isee.nagoya-u.ac.jp/vlist). We acknowledge the use of NASA/GSFC's Space Physics Data Facility's OMNIweb or CDAWeb service, and OMNI data. We thank the Wilcox Solar Observatory (WSO) for providing open access to the magnetograph data, and the Royal Observatory of Belgium for providing the sunspot number data. This research was partially supported by JSPS KAKENHI Grant-in-Aid for Scientific Research(C) (21K03640).

ORCID iDs

Munetoshi Tokumaru https://orcid.org/0000-0002-2982-1887
Ken'ichi Fujiki https://orcid.org/0000-0002-7060-3750
Kazumasa Iwai https://orcid.org/0000-0002-2464-5212

References

Asai, K., Kojima, M., Tokumaru, M., et al. 1998, JGR, 103, 1991
Bame, S. J., McComas, D. J., Barraclough, B. L., et al. 1992, A&AS, 92, 237
Bruno, R., & Carbone, V. 2005, LRSP, 2, 4
Coles, W. A. 1978, SSRv, 21, 411
Fox, N. J., Velli, M. C., Bale, S. D., et al. 2016, SSRv, 204, 7
Fujiki, K., Kojima, M., Tokumaru, M., et al. 2003, AnGeo, 21, 1257
Hakamada, K., & Kojima, M. 1999, SoPh, 187, 115
Hewish, A., Scott, P. F., & Wills, D. 1964, Natur, 203, 1214
Hoeksema, J. T. 1995, SSRv, 72, 137
Jackson, B. V., Hick, P. L., Kojima, M., & Yokobe, A. 1998, JGR, 103, 12049
Janardhan, P., Bisoi, S. K., Ananthakrishnan, S., et al. 2015, JGRA, 120, 5306
King, J. H., & Papitashvili, N. E. 2005, JGRA, 110, A02104
Kojima, M., & Kakinuma, T. 1990, SSRv, 53, 173
Kojima, M., Tokumaru, M., Fujiki, K., Hayashi, K., & Jackson, B. V. 2007, A&AT, 26, 467
Kojima, M., Tokumaru, M., Watanabe, H., et al. 1998, JGR, 103, 1981
Le Chat, G., Issautier, K., & Meyer-Vernet, N. 2012, SoPh, 279, 197
McComas, D. J., Bzowski, M., Dayeh, M. A., et al. 2020, ApJS, 248, 26
McComas, D. J., Ebert, R. W., Elliott, H. A., et al. 2008, GeoRL, 35, L18103
Mullan, D. J. 1983, ApJ, 272, 325
Müller, D., Cyr, O. C., St., Zouganelis, I., et al. 2020, A&A, 642, A1
Neugebauer, M. 1992, in Solar Wind Seven Coll., ed. E. Marsch & R. Schwenn (Oxford: Pergamon), 69
Nolte, J. T., Krieger, A. S., Timothy, A. F., et al. 1976, SoPh, 46, 303
Richardson, J., & Wang, C. 1999, GeoRL, 26, 561
Schwenn, R., & Marsch, E. 1991, PCS, 21, 159
Shoda, M., Suzuki, T. K., Asgari-Targhi, M., & Yokoyama, T. 2019, ApJL, 880, L2
Sokół, J. M., McComas, D. J., Bzowski, M., & Tokumaru, M. 2020, ApJ, 897, 179
Steinitz, R., & Eyni, M. 1980, ApJ, 241, 417
Svalgaard, L., Duvall, T. L. J., & Scherrer, P. H. 1978, SoPh, 58, 225
Tokumaru, M. 2013, PJAB, 89, 67
Tokumaru, M., Fujiki, K., & Iju, T. 2015, JGRA, 120, 3283
Tokumaru, M., Kojima, M., & Fujiki, K. 2010, JGRA, 115, A04102
Tokumaru, M., Kojima, M., & Fujiki, K. 2012, JGRA, 117, A06108
Tokumaru, M., Satonaka, D., Fujiki, K., Hayashi, K., & Hakamada, K. 2017, SoPh, 292, 41
Tokumaru, M., Shimoyama, T., Fujiki, K., & Hakamada, K. 2018, JGRA, 123, 2520
Wang, Y. M., & Sheeley, N. R. J. 1990, ApJ, 355, 726
Young, A. T. 1971, ApJ, 168, 543